AIAA Aviation Forum and ASCEND co-located Conference Proceedings
29 July - 2 August 2024, Las Vegas, Nevada
AIAA AVIATION FORUM AND ASCEND 2024

10.2514/6.2024-3696

High-Fidelity CFD Verification Workshop 2024: Post-Workshop Mesh Motion Summary

Nathan A. Wukie*
Air Force Research Laboratory, Wright-Patterson AFB, United States

Krzysztof Fidkowski†
University of Michigan, Ann Arbor, MI, USA

Per-Olof Persson‡
University of California, Berkeley, Berkeley, CA, United States
Lawrence Berkeley National Laboratory, Berkeley, Berkeley, CA, United States

Takeshi R. Fujimoto§, Z.J. Wang¶
University of Kansas, Lawrence, KS, USA

James Gabbard‖, Wim M. van Rees**
Massachusetts Institute of Technology, Cambridge, MA, USA

This paper reviews the result of the Mesh Motion test suite, assembled as part of the 2024 High Fidelity CFD Verification Workshop. This test suite extends studies of two geometries introduced in the previous iteration of the workshop, internal flow in a deforming cylinder geometry and external flow over a heaving and pitching airfoil. The extensions consist of redefining the cylinder motion to study volume scaling terms, to break problem symmetries, and to study the convergence of spatial and temporal errors and their impact on long-time stability of both cases. Five groups participated in the workshop, using various spatial and temporal discretizations. The results indicate agreement between several groups to a greater extent than in previous workshops. The discussion identifies reasons for differences and makes suggestions for further studies.

I. Introduction

The most recent High-Fidelity Computational Fluid Dynamics (CFD) Verification Workshop, previously known as the High-Order Workshop [1], was held at the 2024 AIAA SciTech conference. The goals of this workshop are; (1) to support new research in the area of high-fidelity CFD methods; (2) to identify pacing items for high-fidelity methods; and (3) to facilitate collaboration among CFD researchers and practitioners.

*Research Engineer, Multidisciplinary Science & Technology Center, Air Force Research Laboratory, AIAA Senior Member.
†Professor, Department of Aerospace Engineering, University of Michigan, AIAA Associate Fellow.
‡Professor, Department of Mathematics, University of California, Berkeley
Faculty Scientist, Mathematics Group, Lawrence Berkeley National Laboratory, AIAA Senior Member.
§Graduate Student, Department of Aerospace Engineering, University of Kansas
¶Spahr Professor, Department of Aerospace Engineering, University of Kansas, AIAA Fellow.
‖Graduate Student, Department of Mechanical Engineering, Massachusetts Institute of Technology
**Associate Professor, Department of Mechanical Engineering, Massachusetts Institute of Technology

The workshop consists of several test suites, each of which addresses a broad area relevant to CFD. One of these suites concerns mesh motion, and this is the topic of the present paper.

Fluid problems with moving or deforming domains are found in many aerospace applications, such as fluid-structure interaction, turbomachinery, store separation, and rotor-craft simulations. As part of the High-Fidelity CFD Verification Workshop, the Mesh Motion suite of problems supports code verification activities and seeks to resolve outstanding technical challenges, including data-set agreement, observed rates-of-convergence, and long-time stability. The suite tests the accuracy of flow solvers for problems with moving and deforming domains. For the last two workshops, the suite has included two canonical classes of problems: one involving a deforming cylinder and the other a moving airfoil [2]. In the latest iteration, we have evolved the test suite to target volume scaling terms, to break problem symmetries, and to study the convergence of spatial and temporal errors and their impact on long-time stability.

In the following sections, the moving cylinder and airfoil test cases are presented along with their extensions for the most recent workshop. The submissions of the participants are described, including their discretization and treatment of mesh motion. A comparison of the results from all the groups identifies similarities and areas in need of further investigation. Furthermore, the discussion suggests additional directions in which the test suite can evolve for the next workshop.

II. Mesh motion overview

Due to the difficulty in demonstrating agreement between different groups and high-order convergence for moving boundary problems, we have continued to include flow inside a moving and deforming cylinder in addition to flow over a dynamic NACA0012 airfoil. Furthermore, a more complex combined motion for the cylinder has been employed for the latest workshop. For the sake of completeness, both cases are summarized next.

A. Flow in a cylinder

The reference geometry for this problem is a circular cylinder for which several types of motion are prescribed. The center of motion coincides with the geometric center of the cylinder, and the fluid domain of interest is the cylinder interior volume. Figure 1 shows a diagram of the problem geometry and the fluid domain.

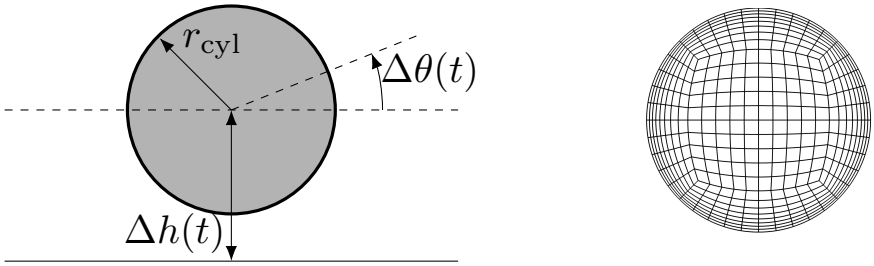

(a) Geometry diagram. **(b) Fluid domain.**

Figure 1: Cylinder problem description.

1. *Cylinder test cases*

Two cylinder test cases are defined. Cylinder Case 1 is a short-time version of the 2022 Cylinder Motion-4, extended to include non-unit geometry mapping Jacobian. Wall boundary conditions are used. Cylinder Case 2 is a long-time study designed to measure the buildup of any errors associated with not satisfying the geometric conservation law.

Relevant constants for all motions are listed in Table 1. A_θ is a rotation amplitude, A_a is an amplification factor for the deformation of a circle into an ellipse, A_g is a volume deformation amplitude, and r_{cyl} is the initial radius of the cylinder for all motions. The transformation of the cylinder deforming into an ellipse such that the interior area remains constant during deformation is facilitated by the function

$$\psi(t) = 1 + (A_a - 1)\alpha(t) \tag{1}$$

r_{cyl}	0.5
A_θ	π
A_a	1.5
A_g	0.15

Table 1: Cylinder motion constants.

which varies from 1 to A_a over $t = [0, 2]$, where $\alpha(t)$ is a time-activation function that is defined differently for each test case in the sections below. Next, a parameterized function η is defined as

$$\eta(\lambda, \omega, \tau) = \sin\left(\omega\lambda + \tau\left(1 - \cos\left(\omega\lambda\right)\right)\right) \tag{2}$$

which is designed to break spatial and temporal symmetries due to the fact that the integral of η over a period ω does not equal 0 for appropriate values of τ. The parameter λ represents the independent variable (e.g. t or θ) whereas ω and τ represent the function frequency and shape characteristics. A subsequent function f_g is defined here to prescribe a deformation that ensures non-unit geometry mapping Jacobians ($g \neq 1$), while utilizing the η function to break spatial and temporal symmetries. This is given as

$$f_g(t, r_0, \theta_0) = \left(16r_0^4 + \frac{t^6}{t^6 + 0.01}\eta(t, 10, 0.7)\left(\cos\left(32\pi r_0^4\right) - 1\right)\right)\eta(\theta_0, 1, 0.7) \tag{3}$$

which was designed with the following properties in mind:

1. Initial prescribed deformation on the cylinder boundary $r_0 = 0.5$ at time $t = 0$, but the boundary deformation is not time-varying. In this way, non-trivial ($g \neq 1$) deformations exist on the wall boundary, yet the static nature of the deformation function on the wall ensures the physical problem is not modified; allowing data to be compared against prior workshop results.
2. Symmetry-breaking spatial perturbation $\eta(\theta_0, 1, 0.7)$.
3. Symmetry-breaking temporal perturbation $\eta(t, 10, 0.7)$.
4. Smooth start-up rapidly reaching an asymptotically periodic region around $t = 1$ via window function $t^6/(t^6 + 0.01)$.

The prescribed deformation takes the form of a perturbation in θ as

$$\theta_g(t, r_0, \theta_0) = \theta_0 + A_g f_g(t, r_0, \theta_0) \tag{4}$$

A composite motion (translation, rotation, deformation) is then formed by representing primitive motions as transformation matrices and composing them by matrix multiplication. Note, translation is not a linear transformation in (x, y)-space. However, translation can be accommodated by augmenting the transformation to $(x, y, 1)$-space. In contrast to the previous workshop motion where the primitive motions were operating on (x_0, y_0), the new motion operates on the deformed coordinates $(r_0\cos(\theta_g), r_0\sin(\theta_g))$. The prescribed motion is composed as

$$\begin{bmatrix} x \\ y \\ 1 \end{bmatrix} = \begin{bmatrix} 1 & 0 & 0 \\ 0 & 1 & \alpha(t) \\ 0 & 0 & 1 \end{bmatrix} \begin{bmatrix} \cos(A_\theta\alpha(t)) & -\sin(A_\theta\alpha(t)) & 0 \\ \sin(A_\theta\alpha(t)) & \cos(A_\theta\alpha(t)) & 0 \\ 0 & 0 & 1 \end{bmatrix} \begin{bmatrix} \psi(t) & 0 & 0 \\ 0 & \frac{1}{\psi(t)} & 0 \\ 0 & 0 & 1 \end{bmatrix} \begin{bmatrix} r_0\cos\left(\theta_g(t)\right) \\ r_0\sin\left(\theta_g(t)\right) \\ 1 \end{bmatrix} \tag{5}$$

2. Cylinder Case 1: short-time composite with deformation extension

The motion for Cylinder Case 1 is defined as a composite of three primitive motions; including translation, rotation, and deformation with the addition of the deformation function (f_g) described above. The time-activation function $\alpha(t)$ for this case is given as

$$\alpha(t) = t^3\left(8 - 3t\right)/16 \tag{6}$$

which varies from 0 to 1 on the interval $t = [0, 2]$. Case 1 shall be run from $t = 0$ until $t = 1$. The intent of this case in the test suite is to break any intrinsic symmetries in the flow field that may cause symmetric error contributions to cancel each other out; causing certain implementation errors to pass a test undetected. Figure 2 shows an example of the short-time problem along with the determinant of the Jacobian mapping g. Figure 2a portrays a notional initial mesh. Note, that the motion includes a deformation at $t = 0$, which is shown in Figure 2b and notable in Figure 2e. The final time $t = 1$ is also shown in Figures 2c and 2f.

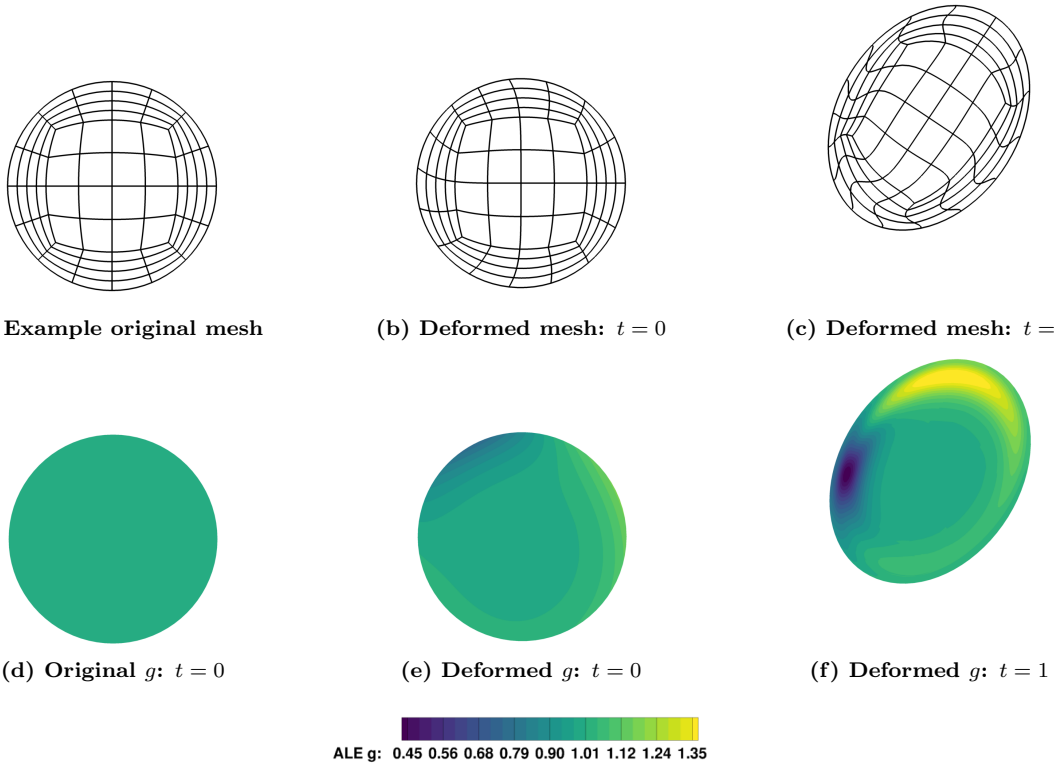

(a) Example original mesh **(b) Deformed mesh: $t = 0$** **(c) Deformed mesh: $t = 1$**

(d) Original g: $t = 0$ **(e) Deformed g: $t = 0$** **(f) Deformed g: $t = 1$**

Figure 2: Cylinder Case 1: short-time version of a composite motion extended for $g \neq 1$

3. Cylinder Case 2: long-time study of conservation

The motion for Cylinder Case 2 has the same form as that of the composite motion for Cylinder Case 1, but with a different $\alpha(t)$ function. To allow for long-time simulations, $\alpha(t)$ is a ramped sine:

$$\alpha(t) = \alpha_{\max} \sin(\omega_\alpha t) \frac{t^6}{t^6 + t_{\text{ref}}^6}, \tag{7}$$

where $\alpha_{\max} = 0.3$, $\omega_\alpha = 6$, and $t_{\text{ref}} = 1$. The purpose of the term with t^6 in the equation is to start the sinusoidal motion slowly and smoothly at $t = 0$. Case 2 shall be run for a longer time, from $t = 0$ until $t = 40$. Running this motion for a long time will test to what extent mass conservation errors, which may arise in formulations that do not explicitly enforce the geometric conservation law [3], build up in the solution.

4. Governing equations and flow conditions

The governing equations for this problem are 2D compressible Navier-Stokes with a constant ratio of specific heats equal to 1.4, a Prandtl number of 0.72 and a constant viscosity. For cases running with wall boundaries, the cylinder interior is prescribed with a no-slip, adiabatic wall boundary condition. The initial condition at time $t = 0$ is given by the conserved-variable state vector

$$\boldsymbol{u}|_{t_0} = [\rho, \rho v_1, \rho v_2, \rho E]|_{t_0} = [1, 0, 0, 50.]$$

For this test suite, a single Reynolds number $Re = 1000$ should be simulated. The reference velocity is chosen to be 1.0 and the reference length scale is the cylinder diameter, $d = 2r_{\text{cyl}} = 1.0$.

B. Heaving-pitching airfoil

These cases involve a NACA 0012 airfoil undergoing a smooth flapping-type motion, starting from rest at zero angle of attack and ending at a one chord length higher position at the end of the motion at time T. Two motions are considered at one Reynolds number, $\mathrm{Re} = 1000$, based on the chord length. The geometry consists of a NACA 0012 airfoil with chord length $c = 1$, with geometry modified to give zero trailing edge thickness:

$$y(x) = \pm 0.6(0.2969\sqrt{x} - 0.1260x - 0.3516x^2 + 0.2843x^3 - 0.1036x^4), \quad x \in [0, 1].$$

The far-field boundary should be located at least 100 chord-lengths away from the airfoil.

1. *Airfoil Motions*

The airfoil undergoes a smooth upward motion of one chord length for the duration of $T = 2$ time units, by heaving and pitching about a point located at the airfoil 1/3 chord location (see figure). We consider two different motions with different properties. The underlying functions for the motions are given here:

$$\alpha(t) = t^3 (8 - 3t) /16$$
$$\beta(t) = -t^6 + 6t^5 - 12t^4 + 8t^3$$

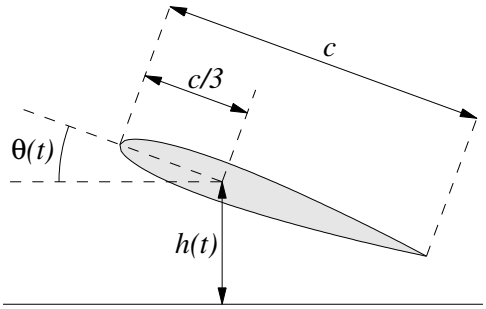

Table 2 presents the two motion descriptions in terms of vertical and angular displacements, where $B_\theta = 80\pi/180$.

	Motion 1	Motion 2
$\Delta h(t)$	$\alpha(t)$	$\alpha(t)$
$\Delta\theta(t)$	0	$B_\theta \cdot \beta(t)$

Table 2: Heaving-pitching airfoil prescribed-motion test cases, $t \in [0, 2]$

2. *Governing equations and flow conditions*

The governing equations for this problem are the 2D compressible Navier-Stokes equations with a constant ratio of specific heats equal to 1.4, a Prandtl number of 0.72 and a constant viscosity. Two boundary conditions are imposed: far-field characteristic conditions at the outer domain and no-slip adiabatic wall condition on the moving airfoil.

The free-stream Mach number is horizontal and two Mach number cases are requested $M_\infty = [0.01, 0.2]$. The Mach number $M = 0.01$ case has been added to approximate incompressibility and facilitate comparison between participants (both for compressible and incompressible methods). The Reynolds number based on the chord of the airfoil is $\mathrm{Re} = 1000$. The initial condition at time $t = 0$ is the steady-state solution for the initial position $h = 0$, $\theta = 0$. To simplify post-processing, we assume convenient units in which the airfoil chord is $c = 1$ and the free-stream density and speed are unity, so that the free-stream conservative state vector is

$$[\rho, \rho u, \rho v, \rho E] = \left[1,\ 1,\ 0,\ 0.5{+}1/[M^2\gamma(\gamma - 1)]\right].$$

III. Participant methodologies

The mesh motion test suite received results from five groups: University of Michigan, University of California - Berkeley, University of Kansas, Air Force Research Laboratory, and the Massachusetts Institute of Technology. Each group has provided a brief description of their methodology, which are described below.

A. University of Michigan

The UM solver, xflow [4], uses a discontinuous Galerkin (DG) finite-element spatial discretization with the Roe convective flux [5] and the second form of Bassi and Rebay [6] for the viscous treatment. The state is approximated on an unstructured mesh using full-order or tensor-product polynomials of order p. The nonlinear solver is a Newton-Raphson method with the generalized minimum residual (GMRES) linear solver, preconditioned by element-line Jacobi or ILU smoothers with a coarse-level correction. In time, the solver supports many discretizations, including diagonally-implicit Runge-Kutta (DIRK) and modified extended backward difference formulas (MEBDF) [7]. Motion of the geometry and mesh is implemented in an arbitrary Lagrangian-Eulerian (ALE) formulation [3, 8], with analytical, blended mappings. The quadrature rules are increased to more accurately integrate the various terms in the discretization, whose nonlinearity increases with that of the mapping. No geometric conservation law is used. Figures 3 and 4 show the first three cylinder and airfoil mesh refinements used to generate the results.

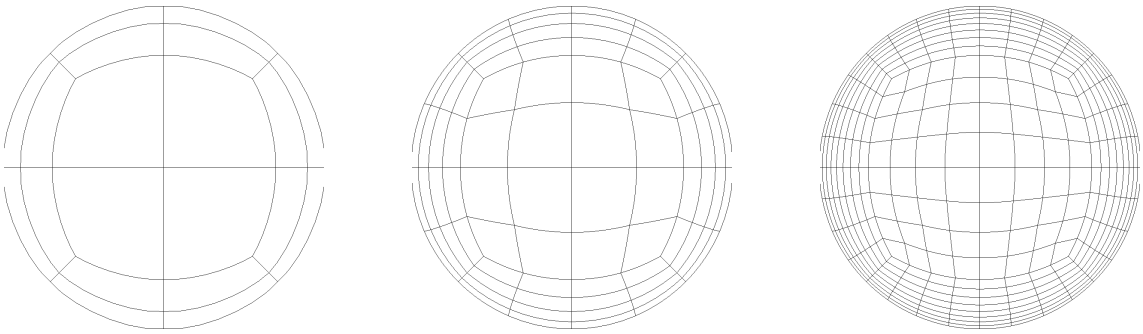

(a) 20 elements **(b) 80 elements** **(c) 320 elements**

Figure 3: Cylinder meshes used by the UM group

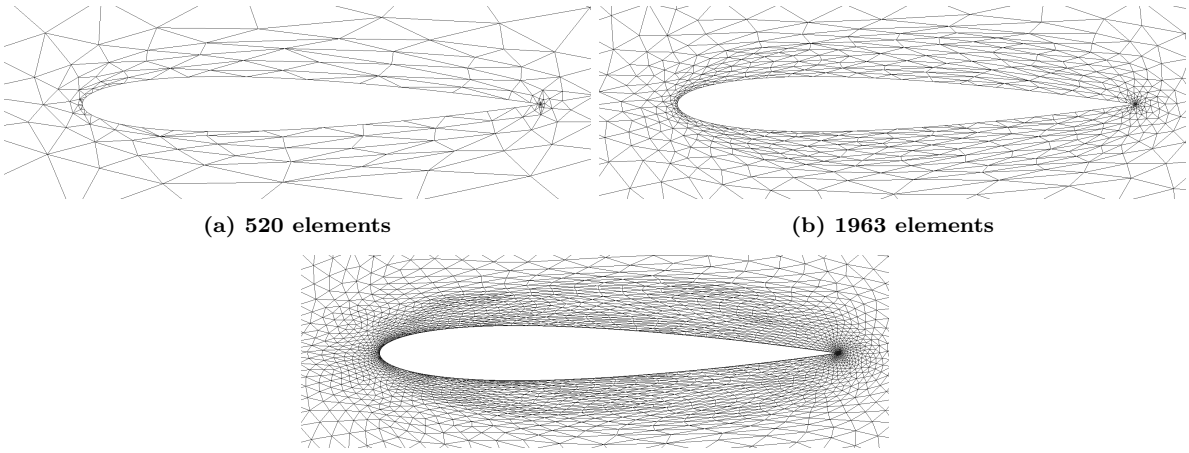

(a) 520 elements **(b) 1963 elements**

(c) 7781 elements

Figure 4: Airfoil meshes used by the UM group

B. University of California, Berkeley

The UCB results are produced using the *3DG package*, with a C++ kernel and interfaces to Python and MATLAB. The discretization is a high-order nodal DG method with the Compact DG method [9] for the viscous terms. The parallel implicit solvers are based on the methodology in [10] with Newton-GMRES solvers, block-ILU preconditioners, Minimum Discarded Fill (MDF) element ordering, and parallelization using MPI and Jacobian-weighted domain partitioning. The deforming domains are handled using the mapping-based ALE formulation in [3]. The curved triangular meshes for the cylinder are produced using an

in-house code, see Figure 5. The airfoil meshes use quadrilateral elements, see Figure 6, and are generated using the Gmsh software [11] combined with in-house routines for boundary layers and element curving.

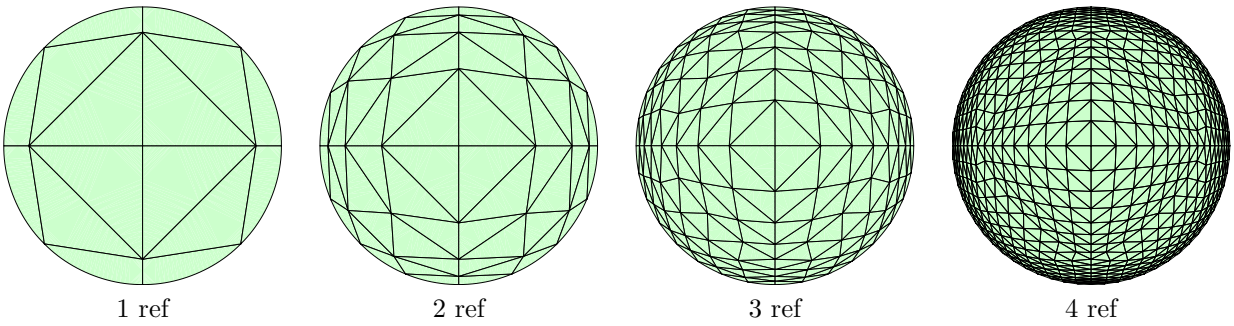

Figure 5: Cylinder meshes used by the UCB group

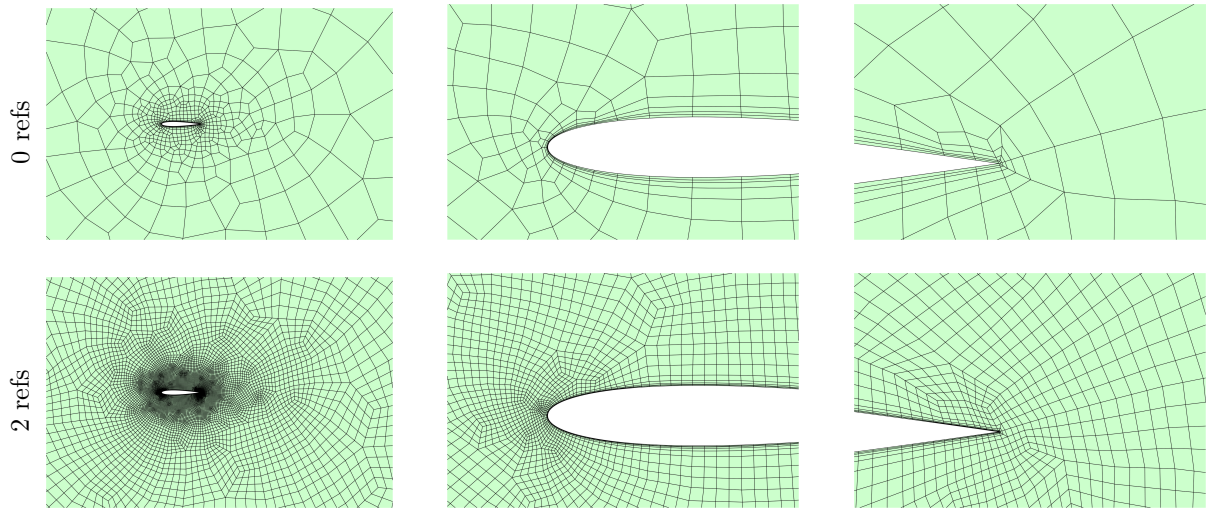

Figure 6: Airfoil meshes used by the UCB group

C. University of Kansas (KU)

The KU flow solver, hpMusic [12], is based on the flux reconstruction (FR) or correction procedure via reconstruction (CPR) method [13–15]. A review of the FR/CPR method was presented in [16]. Since hpMusic is a general-purpose production large eddy simulation (LES) solver, the time marching scheme involves only two time levels and the geometric conservation law is satisfied. This requirement also dictates that the scheme can only be at most 2nd-order in time. Given the meshes at time level n and n+1, the grid velocity is computed with these meshes discretely. Also, the mesh at n+1/2 is obtained by averaging the meshes at n and n+1. In the residual evaluation, the metrics at n+1/2 are used to ensure 2nd order accuracy in time. Both explicit and implicit time-integration methods have been implemented in hpMusic. The explicit method is the 2nd-order Runge-Kutta scheme while the implicit method is the Crank-Nicolson scheme with an LU-SGS solver. Sample meshes for the cylinder and the NACA0012 airfoil are displayed in figure 7 and figure 8

D. Air Force Research Laboratory: overset discontinuous Galerkin method

The AFRL methodology employs an overset discontinuous Galerkin spatial discretization, which utilizes a tensor-product Legendre polynomial basis and quadrature-based integration[17]. Diffusion terms are discretized utilizing the second scheme of Bassi and Rebay[6]. For solving problems on moving and deforming

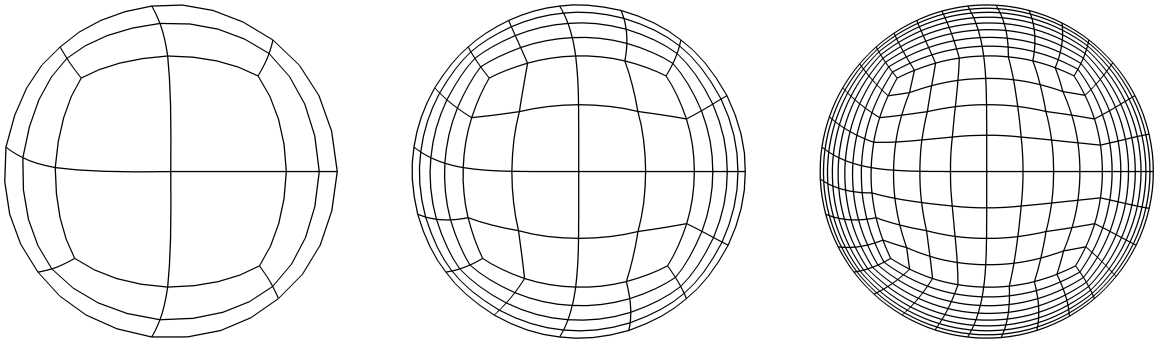

(a) 20 elements **(b) 80 elements** **(c) 320 elements**

Figure 7: Cylinder meshes used by the KU group

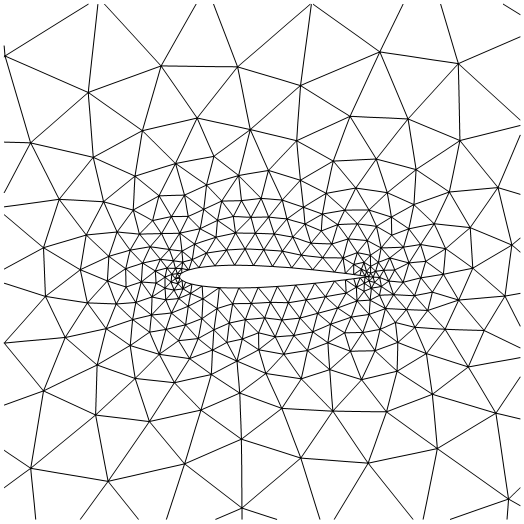

(a) 978 elements

Figure 8: Airfoil meshes used by the KU group

domains an arbitrary Lagrangian-Eulerian (ALE) approach is utilized that follows from the works of Persson et al.[3] and Fidkowski[18]. Displacements and velocities are prescribed directly for all time-levels and no treatment or enforcement of the geometric conservation law is applied. Two unique methodological aspects of the spatial discretization are the treatment for overset boundaries as well as the treatment for the gradient of the determinant of the ALE deformation mapping Jacobian (g). The treatment of advective terms across abutting overset boundaries is identical to the interior scheme. However, the treatment of diffusion terms follows the approach of Galbraith[19] and it is not identical to the interior scheme and this approach is not well-characterized for the ALE methodology. The gradient of the determinant of the ALE mapping Jacobian (∇g) is computed by first projecting g to the modal basis. The modal representation is then differentiated and evaluated for ∇g. This approach introduces a component of error due to the approximation of g in a truncated modal basis. The impact of this approach on overall accuracy for the ALE method is unclear. A third-order, diagonally-implicit Runge-Kutta method is used for temporal discretization and marching in time. The nonlinear discrete systems are solved using Newton's method with a flexible version of the generalized minimum residual (FGMRES) linear solver and incomplete lower-upper factorization preconditioners with zero fill-in (ILU0) and restricted additive Schwarz preconditioning across partition boundaries.

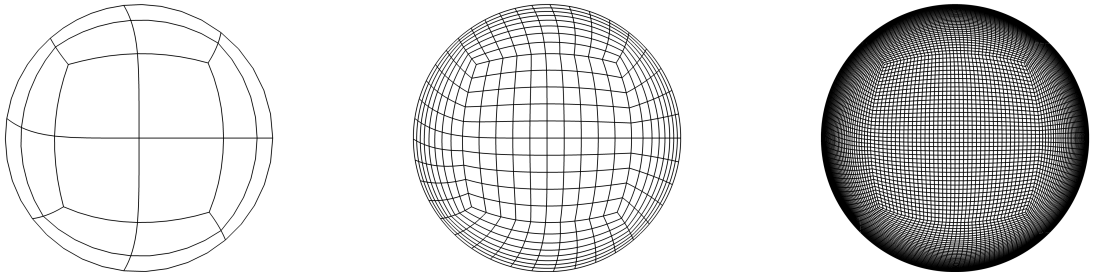

(a) 20 elements - $h0$ **(b) 420 elements -** $h2$ **(c) 6720 elements -** $h4$

Figure 9: Multi-block Cylinder meshes used by the AFRL group (after displacement applied at $t = 0$). Four grid blocks oriented across vertical and horizontal symmetry boundaries.

E. Massachusetts Institute of Technology: sharp immersed finite difference method

The MIT group's solver is based on the vorticity-velocity formulation of the incompressible Navier-Stokes equations, discretized using a conservative second-order finite difference scheme. The no-slip boundary conditions on the body are enforced using a second-order sharp immersed interface method. The discretized vorticity and velocity are defined on a uniform rectangular computational grid, and integrated in time using a third-order low-storage Runge Kutta scheme. For the airfoil case, free-space domain boundary conditions are enforced by computing the stream function field from a convolution of the vorticity field with an unbounded Lattice Green's Function kernel. To enforce no-through flow, the Dirichlet boundary condition on the streamfunction ψ is obtained by integrating $\partial_s \psi = \boldsymbol{u}_s \cdot \boldsymbol{n}$ along the surface. Details of the methodology are provided in [20, 21].

For the cylinder motions defined here, we derived some additional expressions to express the boundary kinematics in Eulerian form. In addition, we compute forces and work integrands from a set of boundary integrals that do not require explicit knowledge of the pressure field, which is advantageous in the vorticity-velocity formulation. These derivations and expressions are provided in the Appendix. For these simulations, we use a rectangular domain of size $1.5D \times 2D$, with $D = 2r_0$ the reference diameter of the cylinder. The reported resolutions vary from $D/h = 128$ to $D/h = 1024$, with h the linear grid spacing. The timestep varies accordingly associated with the CFL condition, so that the number of timesteps is resolution-dependent. The $nDOF$ quantity reported in convergence plots below is computed as the total number of grid points in the rectangular domain.

For the airfoil motion, the boundary conditions on ψ are readily obtained given the imposed rigid-body motion. For this case, forces are obtained from a control volume analysis as described in [20, 21]. Moreover, instead of initializing the airfoil simulations from a steady-state solution as in the workshop description, we simulate an impulsively started flow for $t = 3$ time units without airfoil motion, before starting the motion. For all airfoil simulations, we use a rectangular domain of size $7c \times 3c$, with c the airfoil chord length. The

reported resolutions vary from $c/h = 192$ to $c/h = 512$ with h the linear grid spacing. Similar to the cylinder, the $nDOF$ quantity reported in convergence plots below is computed as the total number of grid points in the rectangular domain.

IV. 2024 Workshop Results

The mesh motion test suite resources, data-sets, and reference material are all hosted in a git repo on GitHub: https://github.com/HighFidelityCFDVerificationWorkshop/2024MeshMotion.

A. Flow in a cylinder

Tables 3 – 5 list the metadata for the datasets submitted by each participant. This includes time-integration scheme, number of time-steps in a dataset, mesh-sizes, and the number of degrees of freedom being solved for in a computational unit for different spatial orders of accuracy.

	Time Integrator	Order	$t0$	$t1$	$t2$	$t3$	$t4$	$t5$	$t6$
U. of Michigan	MEBDF3	4	64	128	256	512	1024		
U.C. Berkeley	DIRK3	3	64	128	256	512	1024	2048	4096
University of Kansas	CN-LUSGS	2	1600	25600	51200				
AFRL	DIRK3	3	10	20	40	80	160	320	
MIT (Incompressible)	LS-RK3 (explicit)	3	unreported						

Table 3: Cylinder data-set time-steps per time-index meta-data

	$h0$	$h1$	$h2$	$h3$	$h4$	$h5$
U. of Michigan	20	80	320	1280		
U.C. Berkeley	28	96	384	1536	6144	24576
University of Kansas	28	96	352	1344	5248	
AFRL	20	105	420	1680	6720	26880
MIT (Incompressible)	49152	196608	786432	3145728		

Table 4: Cylinder mesh-size per mesh-index meta-data

	$p1$	$p2$	$p3$	$p4$
U. of Michigan	4	9	16	25
U.C. Berkeley	3	6	10	
University of Kansas		9	16	25
AFRL	4	9		
MIT (Incompressible)	1			

Table 5: Degrees of freedom per computational unit (e.g. DOF/element) for prescribed spatial accuracy

1. *Cylinder Motion 1: short-time composite with deformation extension*

The reference integrated outputs for Cylinder Motion-1 from each participant are summarized in Table 6. A significant achievement is that three groups agree to 5-digits for Y-Impulse and to 6-digits for Work, which is an improvement over agreement achieved in previous workshops. Additionally, the University of Kansas methodology has significant differences relative to the U.C. Berkeley and University of Michigan approaches, which are very similar to each other. Obtaining such strong agreement between approaches with significant methodological differences further strengthens the workshop results. This test case is also more complex

than previous iterations of the workshop due to its more complicated interior prescribed deformation. The MIT contribution is an incompressible result, which is a useful reference point for future studies, but without a second incompressible data-set we are unable to make comparisons for the accuracy of this result.

	Y-Impulse	Work
U. of Michigan	**-0.591592**227558552	**-0.30631**48341462194
U.C. Berkeley	**-0.591592**091988115	**-0.30631**47255793583
University of Kansas	**-0.59159**1980034782	**-0.30631**44309126535
Air Force Research Laboratory	**-0.591**606196358035	**-0.306**2983580802984
MIT (Incompressible)	-0.5886924434684133	-0.28786809721431866

Table 6: Cylinder Motion-1 Integrated Quantities

Figure 10 shows spatial and temporal convergence datasets that measure the error in integrated outputs as spatial and temporal discretizations are refined. The truth-values utilized in order to measure error were obtained from the reference dataset contributed by U.C. Berkeley since it was the most spatially and temporally resolved. The convergence results from U.C. Berkeley and the University of Michigan exhibit similar convergence characteristics. There is a clear improvement in spatial convergence for those datasets going from P1 to P2 results. However, it is unclear if significant benefit is observed in spatial convergence for P3 and higher datasets. A similar effect is observed in the University of Kansas datasets, where a significant improvement in spatial convergence is observed going from P2 to P3 results. However, the K.U. P4 results do not exhibit an improvement in spatial convergence over the P3 dataset. Other works have demonstrated clear benefit of higher-order spatial accuracies for moving-domain problems, which may indicate that the stalled spatial order of convergence is related to the problem description. The AFRL dataset exhibits spatial convergence, but at a noticeably degraded rate in comparison to the other participant datasets. In data analysis, it was noted that the AFRL data set is not conserving mass, which is an outstanding issue. As described in the previous section, the AFRL methodology has several differences related to handling of interior deformation, which may be a source of unresolved error, which were not apparent in previous workshops that utilized a simpler form of interior deformation. Figure 22 in Appendix A shows the spatial convergence studies broken out by participant for improved clarity.

Time-histories for Y-Force and the Work integrand are presented in Figure 11. Note, that these histories do not exhibit symmetries that would result in zero or very small integrated outputs that are more challenging to assess convergence. This is by design and an improvement in the present workshop test case over iterations of this problem in previous workshops. All participant datasets exhibit excellent agreement in the presented time-histories.

2. Cylinder Motion 2: long-time study of conservation

The Motion-2 long-time version of the cylinder problem was initially proposed in order to study geometric conservation law (GCL) and aspects of GCL across varying spatial and temporal resolutions. However, it was discovered that for a problem consisting of strictly wall boundary conditions (i.e. no inflow or outflow boundary conditions that exchange mass with some exterior state) overall mass is strictly conserved. Pointwise errors in conservation may exist as a result of deformations (depending on particular approach and methodology), however overall mass should be conserved and constant over time. As a result, no global conservation error exists that could accumulate to drive an instability that would cause the numerical problem to blow up. In the end, there was very little remaining from the original set of objectives for this problem that were left to study. Two participants submitted dataset contributes and their reference values for integrated quantities are presented in Table 7. Only a single digit of agreement is observed in this case. The driving reason for discrepancy is the much longer simulation time and much greater time-resolution requirement. The associated increase in computational time made obtaining a robust set of data for spatial and temporal convergence studies challenging.

Figure 12 presents the spatial convergence study data for the Cylinder Motion-2 problem. Due to the relatively sparse quantity of data for this problem, it is difficult to make strong conclusions other than that a modification of the problem is warranted to support the original goal of studying conservation errors and the impact of GCL associated with moving-mesh formulations.

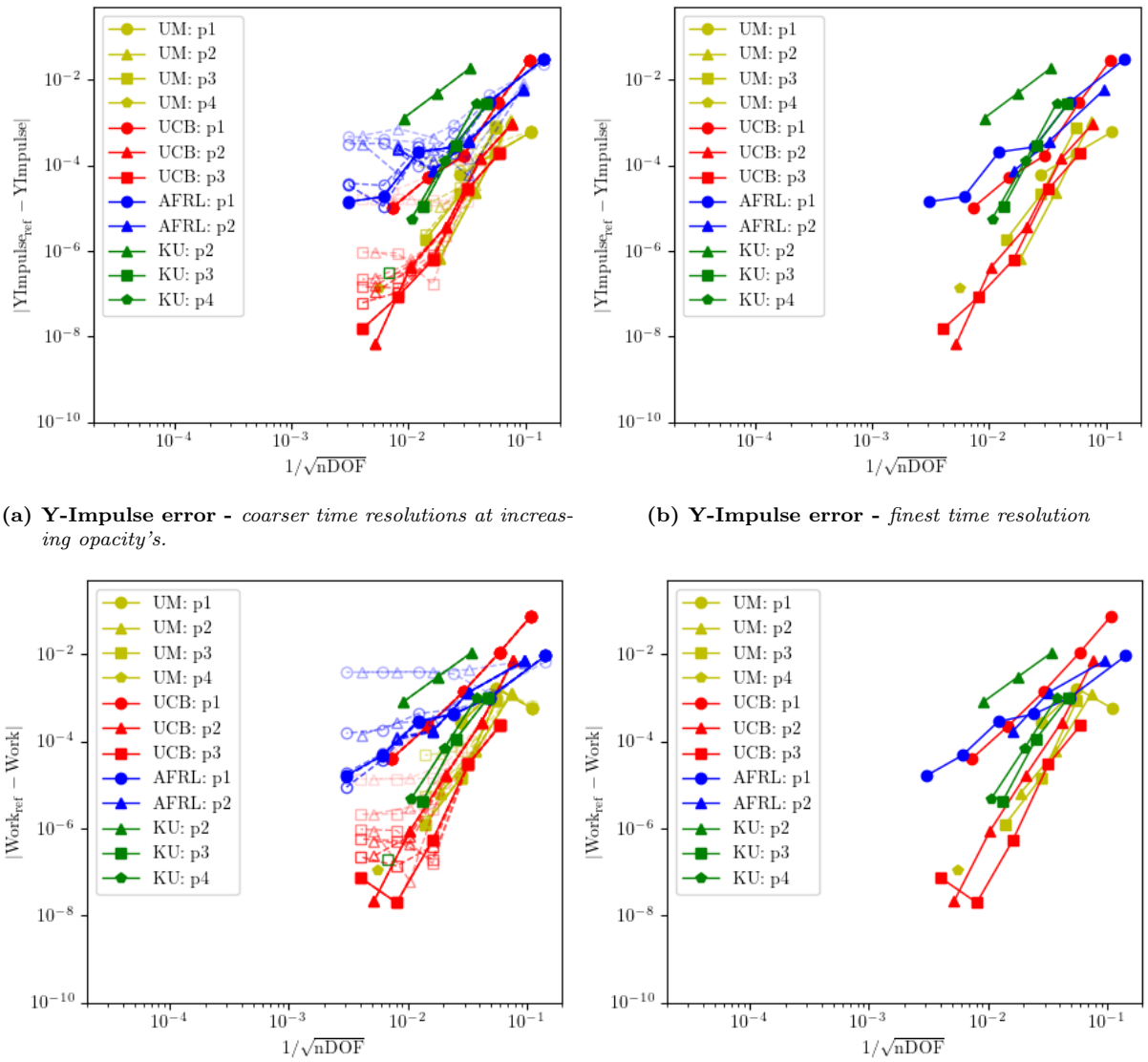

(a) Y-Impulse error - *coarser time resolutions at increasing opacity's.*

(b) Y-Impulse error - *finest time resolution*

(c) Work error - *coarser time resolutions at increasing opacity's.*

(d) Work error - *finest time resolution*

Figure 10: Cylinder Motion-1 Spatial Convergence: *Left column - time-discretization resolution studies plotted as increasingly opaque data sets. Increased opacity associated with less time-resolution. Right column - finest temporal resolution data-sets only for each group. (Truth data set: University of California, Berkeley)*

The Cylinder Motion-2 time-histories for outputs are shown in Figure 13, which show the long-time oscillatory responses. The form of the time-histories agrees well between the University of Michigan and U.C. Berkeley results. However, upon greater inspection, discrepancies exist in the time-history peaks, which is indicative of data-sets that are not completely converged in space or time.

B. Heaving + pitching airfoil

Tables 8 – 10 list the metadata for the airfoil datasets submitted by each participant. This includes time-integration scheme, number of time-steps in a dataset, mesh-sizes, and the number of degrees of freedom being solved for in a computational unit for different spatial orders of accuracy.

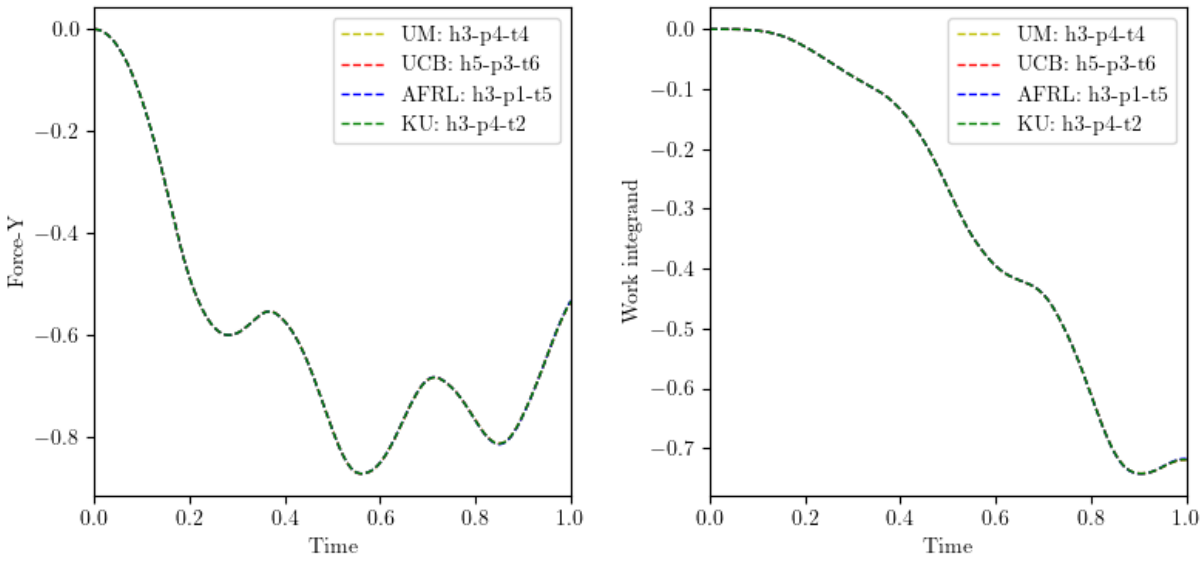

(a) Y-Force **(b) Work integrand**

Figure 11: Cylinder Motion-1 Time Histories (finest space-time resolution data-sets from each participant)

	Y-Impulse	Work
U. of Michigan	**-0.4**326945641157678	**-2**6.59341218705967
U.C. Berkeley	**-0.4**837021105624421	**-2**5.88307185260841

Table 7: Cylinder Motion-2 Integrated Quantities

	Time Integrator	Order	$t0$	$t1$	$t2$	$t3$	$t4$	$t5$
U. of Michigan	ESDIRK5	5	8	16	32	64	128	256
U.C. Berkeley	DIRK3	3	100	200	400	800		
University of Kansas	SSP-RK2	2	2000					
MIT (incompressible)	LS-RK3 (explicit)	3	unreported					

Table 8: Airfoil data-set time-steps per time-index meta-data

	$h0$	$h1$	$h2$	$h3$
U. of Michigan	520	1963	7781	15882
U.C. Berkeley	1150	4232	16240	63632
University of Kansas	978			
MIT (incompressible)	774144	1376256	3096576	5505024

Table 9: Airfoil mesh-size per mesh-index meta-data

1. Airfoil Motion 1: Heaving, $M = 0.2$

The reference integrated quantities from participant datasets are presented in Table 11. Two participant datasets agree to 4 and 5 digits in Y-Impulse and Work outputs respectively. The agreement observed for this case is improved over the iteration of this test case in previous workshops, where the most recent previous study achieved 3-4 digits of agreement.

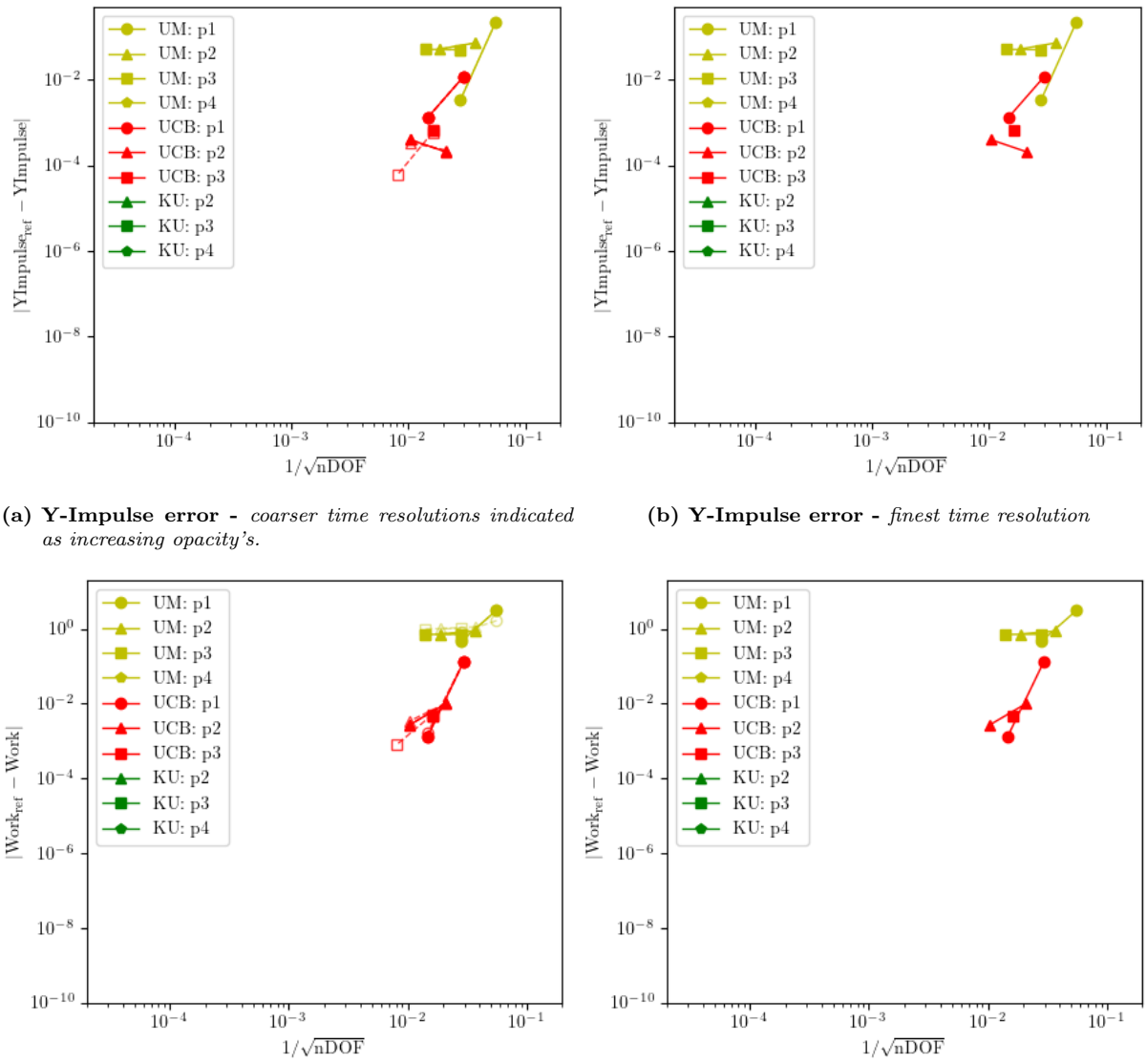

(a) Y-Impulse error - *coarser time resolutions indicated as increasing opacity's.*

(b) Y-Impulse error - *finest time resolution*

(c) Work error - *coarser time resolutions indicated as increasing opacity's.*

(d) Work error - *finest time resolution*

Figure 12: Cylinder Motion-2 Spatial Convergence: *Left column - time-discretization resolution studies plotted as increasingly opaque data sets. Increased opacity associated with less time-resolution. Right column - finest temporal resolution data-sets only for each group. (Truth data set: U.C. Berkeley)*

	$p1$	$p2$	$p3$	$p4$
U. of Michigan	3	6	10	15
U.C. Berkeley	4	9	16	25
University of Kansas	3	6	10	
MIT (incompressible)	1			

Table 10: Degrees of freedom per computational unit (e.g. DOF/element) for prescribed spatial accuracy

Figure 14 shows spatial convergence studies of integrated outputs for the Airfoil Motion-1 (Heaving, Compressible) case. Both University of Michigan and U.C. Berkeley datasets exhibit good and similar

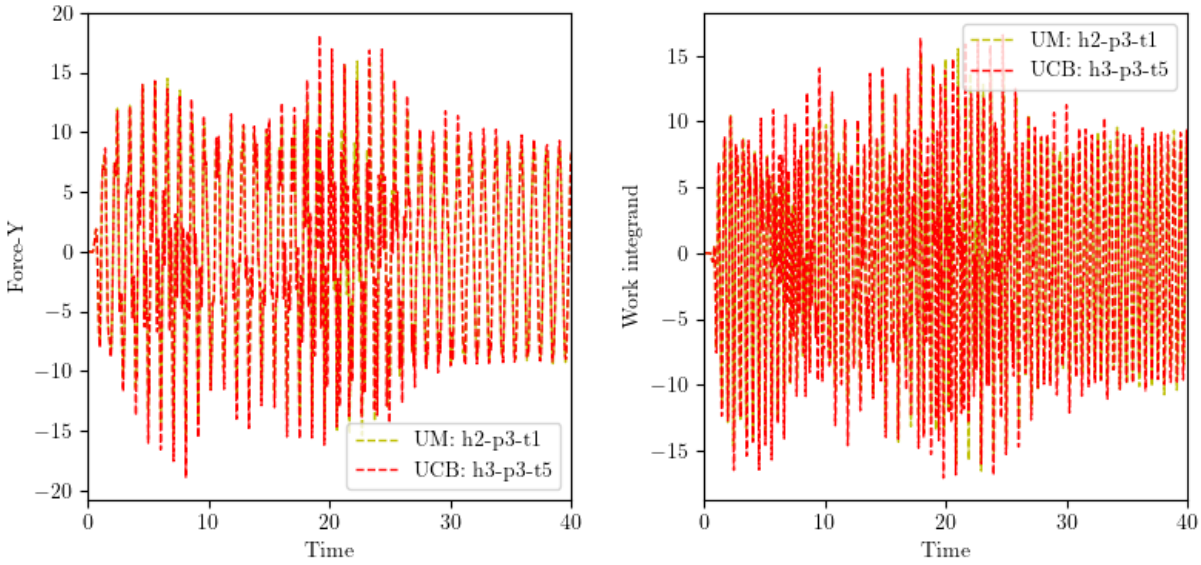

(a) Y-Force **(b) Work integrand**

Figure 13: Cylinder Motion-2 Time Histories (finest space-time resolution data-sets from each participant)

	Data set	Y-Impulse	Work
U. of Michigan	$h3-p3-t3$	**-2.369**2144378342	**-1.6577**365673152817
U.C. Berkeley	$h3-p3-t3$	**-2.369**1970230034	**-1.6577**242816820728
University of Kansas	$h0-p3-t0$	**-2.3**839808944492	**-1.667**2975838590667

Table 11: Airfoil Motion-1 (Heaving, Compressible) Integrated Quantities

convergence behavior. Figure 24 in Appendix A shows the individual convergence datasets broken out more clearly, where it is apparent that the U.C. Berkeley set of data is very strongly time-converged due to only very minor discrepancies observable between the lower time-level datasets plotted. The University of Michigan data set has a more marked manifestation of temporal error in the study. The temporal error can be seen to be strongly reduced in the finest temporal resolution data set, but the temporal error has likely not been completely driven below the spatial discretization error for the finest resolution data set. Finally, the University of Kansas submission for this case did not include a comprehensive set of spatial and temporal resolution data sets for study. Yet, for the resolution of the dataset that was submitted, it aligns well with the error exhibited by the University of Michigan and U.C. Berkeley datasets of similar resolution.

2. Airfoil Motion 2: Heaving + Pitching, $M = 0.2$

The reference integrated quantities from participant datasets are presented in Table 12. Two participant datasets agree to 2 and 3 digits in Y-Impulse and Work outputs, respectively. This level of agreement is inline with results for this test case from previous workshops.

Figure 16 shows spatial and temporal convergence studies for these participant datasets, where it appears that additional spatial and temporal resolution are both required in order to achieve greater agreement and confidence for this test case. Figure 25 in Appendix A shows convergence studies split out for each participant dataset that present spatial and temporal convergence in a clearer manner.

Figure 17 shows reference time-histories for outputs in this test case. For the two participant datasets, excellent agreement is observed and no particular discrepancies are apparent. This motivates the hypothesis that the lack of deep agreement in integrated quantities between participant datasets is likely due to lack of completely converged spatial and temporal discretizations.

	Data set	Y-Impulse	Work
U. of Michigan	$h3-p3-t5$	**0.86**45357323858702	**-2.30**30939915850963
U.C. Berkeley	$h3-p3-t3$	**0.86**29848210439535	**-2.30**42337019067958

Table 12: Airfoil Motion-2 (Heaving+Pitching, $M = 0.2$) Integrated Quantities

3. Airfoil Motion 3: Heaving, $M = 0.01$

The reference integrated quantities from participant datasets are presented in Table 13. Two participant datasets agree to 2 and 1 digits in Y-Impulse and Work outputs respectively. As a low-Mach number problem, this is a new test-case for the test suite. It is worth noting that the U.C. Berkeley contribution is from a compressible solver, which utilizes a tailored preconditioning strategy to converge the low-Mach problem. The MIT dataset in contrast is an incompressible code. To compare, the initial condition for internal energy is adjusted in order to roughly target a $M = 0.01$ flow condition (See Appendix B). For this reason, we do not necessarily expect deep agreement between the contributed datasets in this test case, but it provides a point-of-reference for verifying other incompressible solvers that accommodate mesh motion.

Figure 18 shows convergence histories for this low-Mach, heaving-airfoil test case. The U.C. Berkeley dataset includes a substantial quantity of spatial and temporal resolution data that are converging to a truth value. The incompressible MIT dataset appears to be converging to the highly resolved $Ma = 0.01$ result from the U.C. Berkeley dataset, but at a relatively slow rate. However, the MIT methodology as an immersed geometry method is not as well-suited for evaluating convergence utilizing this approach since there are immersed degrees-of-freedom that are inactive and the uniform mesh is not tailored to a near-body region of interest.

	Data set	Y-Impulse	Work
U.C. Berkeley	$h3-p3-t3$	**-2.2**67601626075732	**-1**.5899144490947763
MIT (incompressible)	$h4-p1-t1$	**-2.2**91792064944407	**-1**.6047038655207724

Table 13: Airfoil Motion-3 (Heaving, $M = 0.01$) Integrated Quantities

4. Airfoil Motion 4: Heaving + Pitching, $M = 0.01$

Only the U.C. Berkeley data set contained results for this test case and reference integrated quantities are presented in Table 14. Just as in the Heaving-$M0.01$ test-case, as a low-Mach number problem, this is a new test-case for the test suite. Since there was only a single group that submitted results, there is relatively little to be said regarding the correctness of the integrated quantities due to lacking an analytical truth-value or truth-by-consensus mechanism. However, Figure 20 shows spatial and temporal convergence histories that indicate this data set does appear to be approaching a converged value. Figure 21 shows the time-history for outputs in this test case, which is useful as a qualitative reference for future groups that might pursue this test-case, but without additional participant data sets to make a comparison against there is not any further conclusion that can be made.

	Y-Impulse	Work
U.C. Berkeley	0.9926402969555639	-2.297032901609105

Table 14: Airfoil Motion-4 (Heaving + Pitching, $M = 0.01$) Integrated Quantities

V. Discussion and Conclusions

A. Summary of accomplishments

The Mesh Motion test suite developed for the 2024 High Fidelity CFD Verification Workshop extended two test cases introduced in a previous workshop: the cylinder and airfoil. The motion of the cylinder was

modified to break symmetries and test non-unity volume scaling terms, while the airfoil case was kept mostly the same with the exception of an additional lower Mach number condition simulation.

Although not all participants ran all of the cases, the test suite can be considered a success in that a high level of agreement was observed among the groups for certain cases. For the Cylinder Motion-1 case, three participants computed outputs that agreed to six digits of accuracy, while for the Airfoil Motion-1 case, four digits of agreement were observed between two participants. Although the cylinder motion was not trivial, the availability of source code with the motion reduced the possibility of implementation errors. In addition to time-integrated quantities, time histories also showed agreement between the participants. The agreement is even more significant when considering that the participants methodologies differed in discretization and treatment of the mesh motion.

B. Challenges and outstanding issues

Mesh motion test cases have been part of the high-order and high-fidelity workshops since the first one in 2012. One of the goals of these workshops has been to study not just the relative merits of high versus low order, but to also assess whether theoretical aspects of high order, including convergence rates, are attained in practical cases. In the present study, high-order convergence was not thoroughly investigated, and care was not taken to ensure that the case specifications were amenable to arbitrarily high-order accuracy. The stagnation of the observed convergence rates in the cylinder case was likely due to high-order derivative discontinuities in the mesh motion specification. The airfoil case further suffers from a geometric singularity at the trailing edge. Adaptive mesh refinement can address the geometric singularities, and future comparisons will ideally incorporate adapted meshes. The mesh motion specification should also be made as smooth as possible to demonstrate optimal rates in space and time.

Another outstanding issue in mesh motion is a study of the importance of a geometric conservation law. Observations by some of the participants suggest that errors introduced by a lack of strict geometric conservation are comparable to other discretization errors due to the inherent finite-dimensional approximation space. In addition, these errors diminish with increasing order. However, possible destabilizing effects of, for example, mass conservation errors, have not been studied in the present suite of cases, at least not to a satisfactory conclusion. Future work should focus on designing long-time simulations in which mass conservation errors play a more prominent role.

An additional topic that warrants further investigation is more complex boundary conditions. These could include walls that are isothermal or on which a non-adiabatic heat flux is imposed, and sliding meshes. Finally, the comparisons would benefit from data obtained from additional discretizations, including established CFD codes.

References

[1] Wang, Z., Fidkowski, K., Abgrall, R., Bassi, F., Caraeni, D., Cary, A., Deconinck, H., Hartmann, R., Hillewaert, K., Huynh, H., Kroll, N., May, G., Persson, P.-O., van Leer, B., and Visbal, M., "High-Order CFD Methods: Current Status and Perspective," *International Journal for Numerical Methods in Fluids*, 2013. doi:10.1002/fld.3767.

[2] Persson, P.-O., Fidkowski, K., and Wukie, N. A., "High-Fidelity CFD Workshop 2022: Mesh Motion," *2021 AIAA SciTech Forum*, 2021. AIAA 2021-1551.

[3] Persson, P.-O., Bonet, J., and Peraire, J., "Discontinuous Galerkin solution of the Navier-Stokes equations on deformable domains," *Computational Methods in Applied Mechanics and Engineering*, Vol. 198, 2009, pp. 1585–1595.

[4] Fidkowski, K. J., "Output-Based Space-Time Mesh Optimization for Unsteady Flows Using Continuous-in-Time Adjoints," *Journal of Computational Physics*, Vol. 341, No. 15, 2017, pp. 258–277. doi:10.1016/j.jcp.2017.04.005.

[5] Roe, P. L., "The use of the Riemann problem in finite difference schemes," *Lecture Notes in Physics*, Vol. 141, No. 5, 1981, pp. 354–359. doi:10.1007/3-540-10694-4.

[6] Bassi, F., and Rebay, S., "Numerical evaluation of two discontinuous Galerkin methods for the compressible Navier-Stokes equations," *International Journal for Numerical Methods in Fluids*, Vol. 40, 2002, pp. 197–207. doi:https://doi.org/10.1002/fld.338.

[7] Cash, J., "The integration of stiff initial value problems in ODEs using modified extended backward differentiation formulae," *Computers & mathematics with applications*, Vol. 9, No. 5, 1983, pp. 645–657. doi: https://doi.org/10.1016/0898-1221(83)90122-0.

[8] Kast, S. M., and Fidkowski, K. J., "Output-based mesh adaptation for high order Navier–Stokes simulations on deformable domains," *Journal of Computational Physics*, Vol. 252, 2013, pp. 468–494.

[9] Persson, P.-O., and Peraire, J., "Newton-GMRES preconditioning for discontinuous Galerkin discretizations of the Navier-Stokes equations," *SIAM J. Sci. Comput.*, Vol. 30, No. 6, 2008, pp. 2709–2733.

[10] Peraire, J., and Persson, P.-O., "The compact discontinuous Galerkin (CDG) method for elliptic problems," *SIAM J. Sci. Comput.*, Vol. 30, No. 4, 2008, pp. 1806–1824.

[11] Geuzaine, C., and Remacle, J.-F., "Gmsh: A 3-D finite element mesh generator with built-in pre-and post-processing facilities," *International journal for numerical methods in engineering*, Vol. 79, No. 11, 2009, pp. 1309–1331.

[12] Wang, Z. J., Li, Y., Jia, F., Laskowski, G., Kopriva, J., Paliath, U., and Bhaskaran, R., "Towards industrial large eddy simulation using the FR/CPR method," *Computers & Fluids*, Vol. 156, 2017, pp. 579–589. doi: https://doi.org/10.1016/j.compfluid.2017.04.026.

[13] Huynh, H. T., "A flux reconstruction approach to high-order schemes including discontinuous Galerkin methods," *18th AIAA computational fluid dynamics conference*, 2007, p. 4079.

[14] Wang, Z., and Gao, H., "A unifying lifting collocation penalty formulation including the discontinuous Galerkin, spectral volume/difference methods for conservation laws on mixed grids," *Journal of Computational Physics*, Vol. 228, No. 21, 2009, pp. 8161–8186. doi:https://doi.org/10.1016/j.jcp.2009.07.036, URL https://www.sciencedirect.com/science/article/pii/S0021999109004239.

[15] Haga, T., Gao, H., and Wang, Z. J., "A high-order unifying discontinuous formulation for the Navier-Stokes equations on 3D mixed grids," *Mathematical Modelling of Natural Phenomena*, Vol. 6, No. 3, 2011, pp. 28–56.

[16] Huynh, H., Wang, Z. J., and Vincent, P. E., "High-order methods for computational fluid dynamics: A brief review of compact differential formulations on unstructured grids," *Computers & fluids*, Vol. 98, 2014, pp. 209–220.

[17] Wukie, N. A., "A discontinuous Galerkin method for turbomachinery and acoustics applications," Ph.D. thesis, University of Cincinnati, 2018.

[18] Fidkowski, K. J., "A hybridized discontinuous Galerkin method on mapped deforming domains," *Computers & Fluids*, Vol. 139, 2016, pp. 80–91.

[19] Galbraith, M. D., "A Discontinuous Galerkin Chimera Overset Solver," Ph.D. thesis, University of Cincinnati, 2013.

[20] Gabbard, J., Gillis, T., Chatelain, P., and van Rees, W. M., "An immersed interface method for the 2D vorticity-velocity Navier-Stokes equations with multiple bodies," *Journal of Computational Physics*, Vol. 464, 2022, p. 111339. doi:https://doi.org/10.1016/j.jcp.2022.111339, URL https://www.sciencedirect.com/science/article/pii/S0021999122004016.

[21] Ji, X., Gabbard, J., and van Rees, W. M., "A sharp immersed method for 2D flow-body interactions using the vorticity-velocity Navier-Stokes equations," *Journal of Computational Physics*, Vol. 494, 2023, p. 112513. doi:10.1016/j.jcp.2023.112513, URL https://doi.org/10.1016%2Fj.jcp.2023.112513.

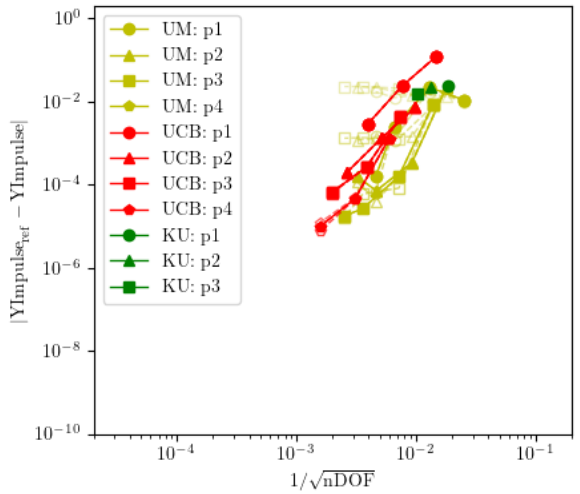

(a) Y-Impulse error - *coarser time resolutions indicated as increasing opacity's.*

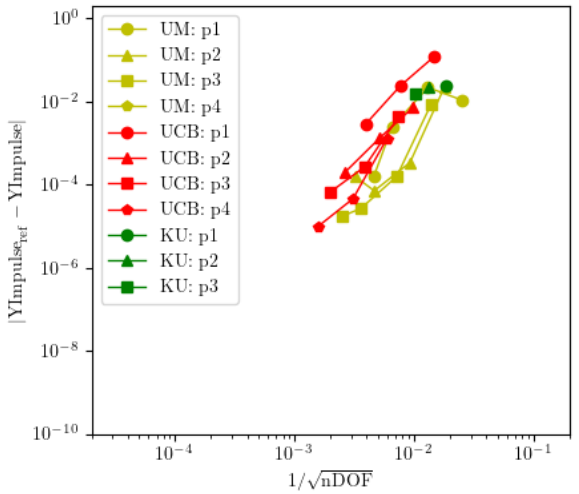

(b) Y-Impulse error - *finest time resolution*

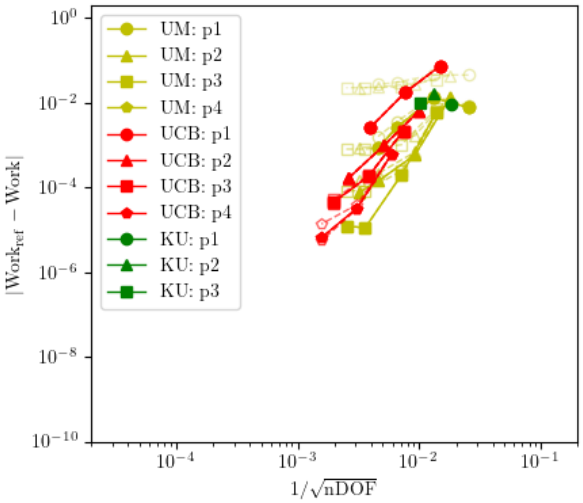

(c) Work error - *coarser time resolutions indicated as increasing opacity's.*

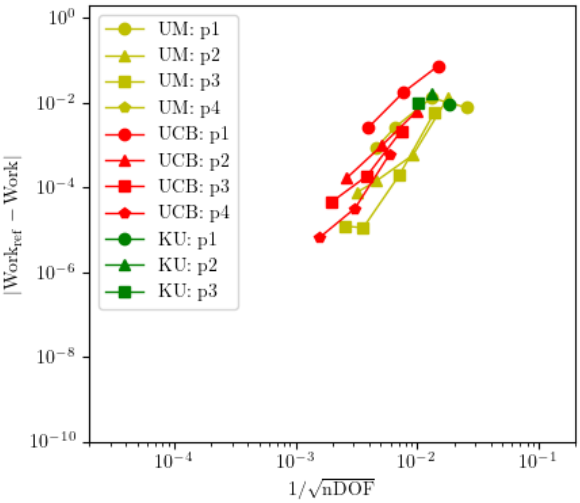

(d) Work error - *finest time resolution*

Figure 14: Airfoil Motion-1 (Heaving, Compressible) Spatial Convergence: *Left column - time-discretization resolution studies plotted as increasingly opaque data sets. Increased opacity associated with less time-resolution. Right column - finest temporal resolution datasets only for each group. (Truth data set: U.C. Berkeley)*

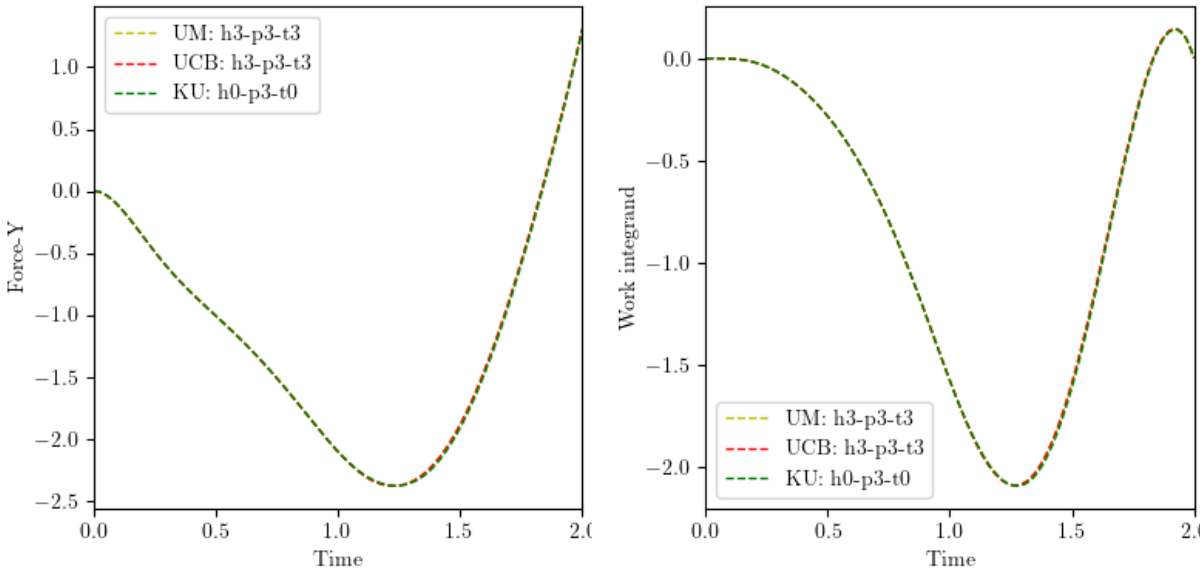

(a) Y-Force **(b) Work integrand**

Figure 15: Airfoil Motion-1 Time Histories (finest space-time resolution data-sets from each participant)

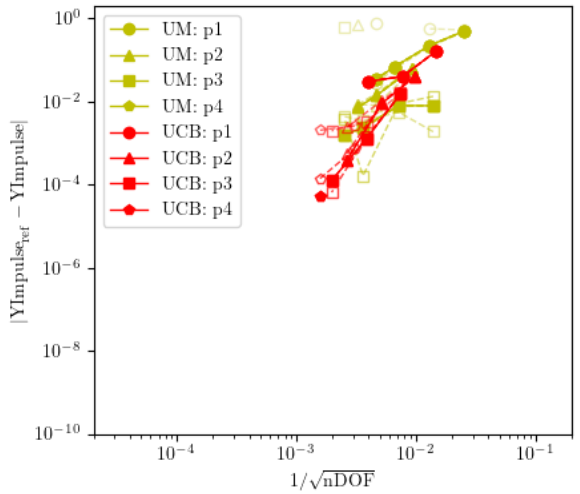

(a) Y-Impulse error - *coarser time resolutions indicated as increasing opacity's.*

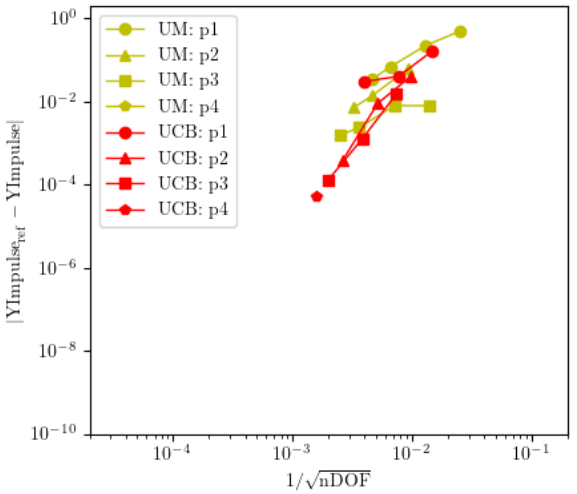

(b) Y-Impulse error - *finest time resolution*

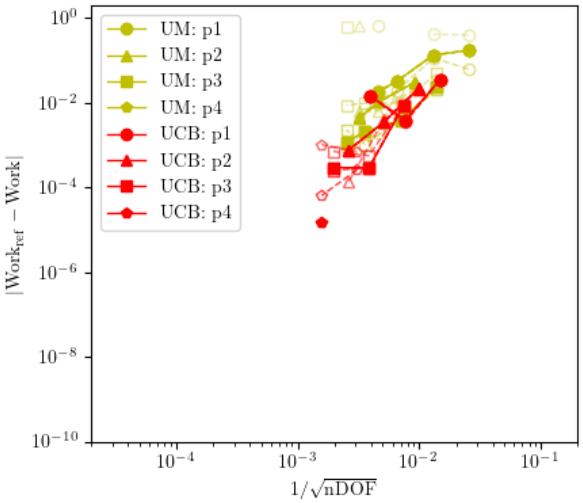

(c) Work error - *coarser time resolutions indicated as increasing opacity's.*

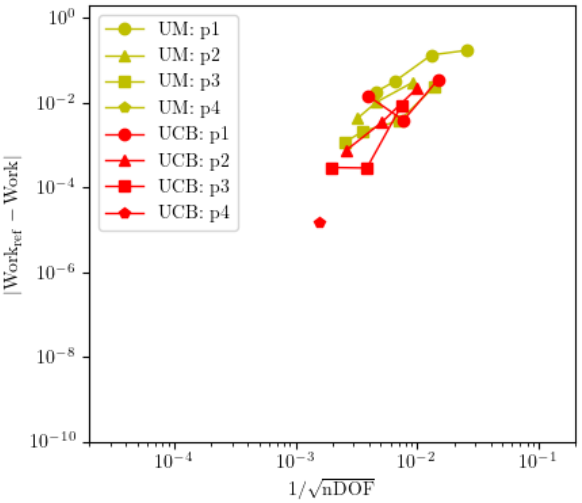

(d) Work error - *finest time resolution*

Figure 16: Airfoil Motion-2 (Heaving + Pitching, $M = 0.2$) Spatial Convergence: *Left column - time-discretization resolution studies plotted as increasingly opaque data sets. Increased opacity associated with less time-resolution. Right column - finest temporal resolution data-sets only for each group. (Truth data set: U. C. Berkeley)*

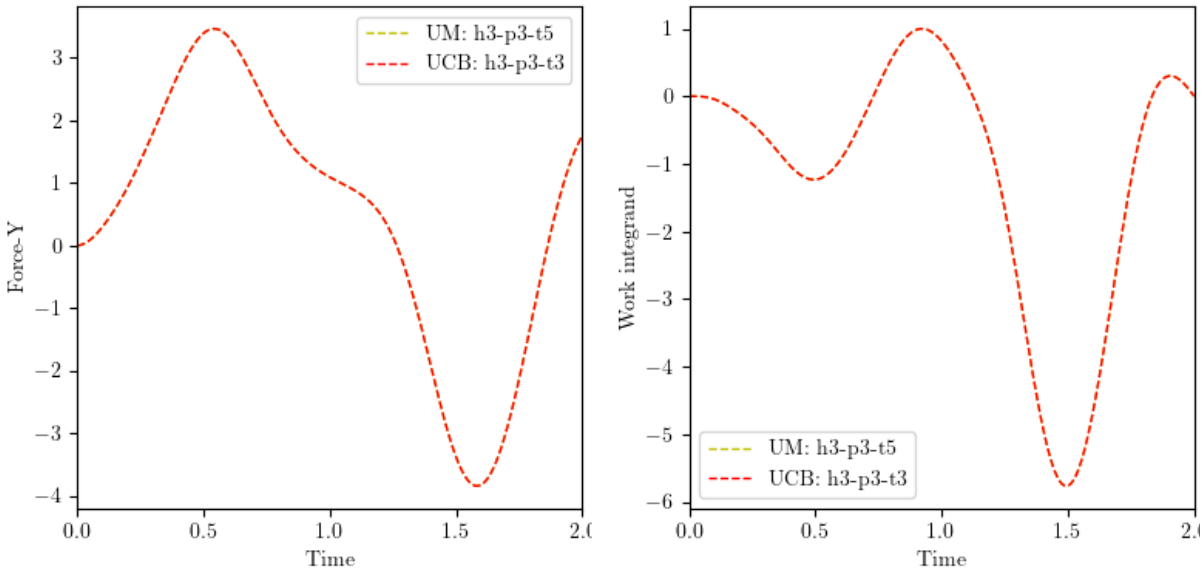

(a) Y-Force **(b) Work integrand**

Figure 17: Airfoil Motion-2 (Heaving + Pitching, $M = 0.2$) Time Histories (finest space-time resolution data-sets from each participant)

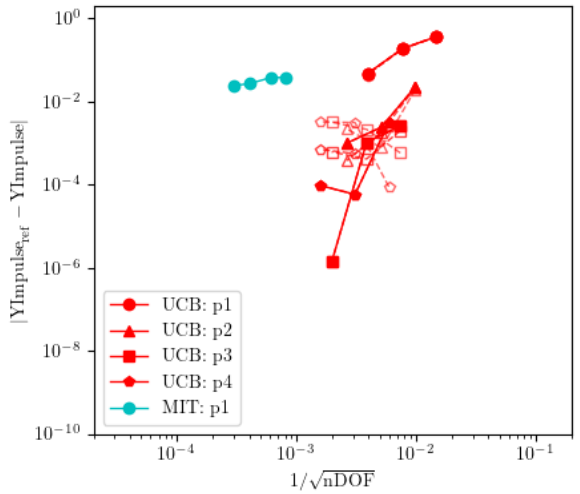

(a) Y-Impulse error - *coarser time resolutions indicated as increasing opacity's.*

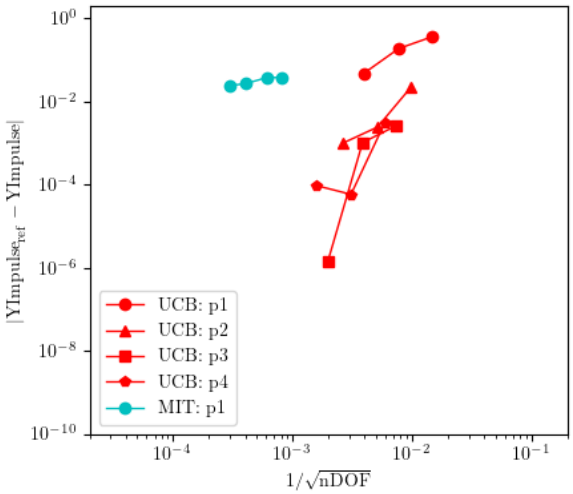

(b) Y-Impulse error - *finest time resolution*

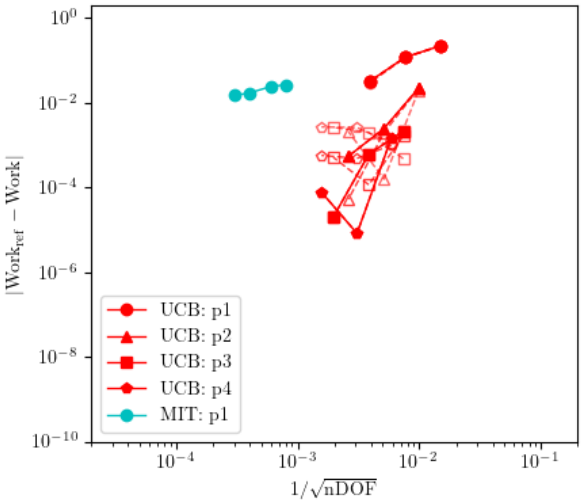

(c) Work error - *coarser time resolutions indicated as increasing opacity's.*

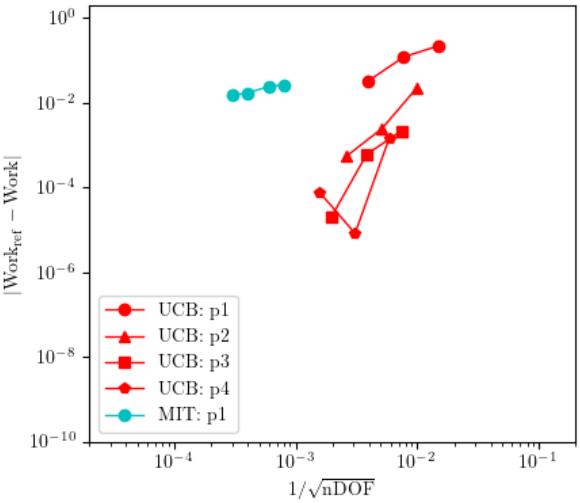

(d) Work error - *finest time resolution*

Figure 18: Airfoil Motion-3 (Heaving, $M = 0.01$) Spatial Convergence: *Left column - time-discretization resolution studies plotted as increasingly opaque data sets. Increased opacity associated with less time-resolution. Right column - finest temporal resolution data-sets only for each group. (Truth data set: U. C. Berkeley)*

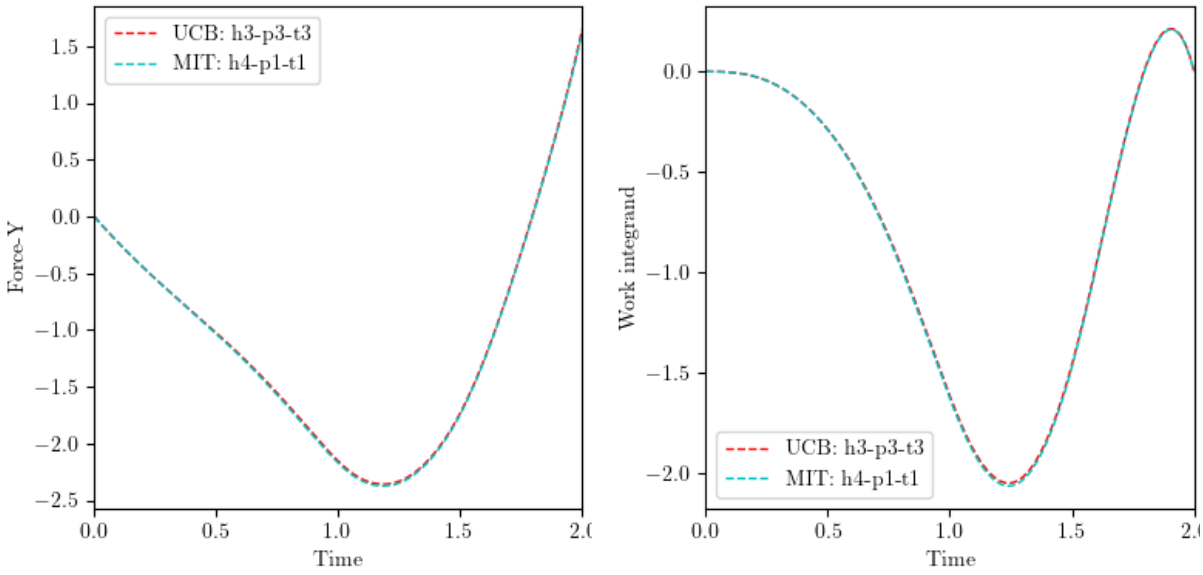

(a) Y-Force **(b) Work integrand**

Figure 19: Airfoil Motion-3 (Heaving, $M = 0.01$) Time Histories (finest space-time resolution data-sets from each participant)

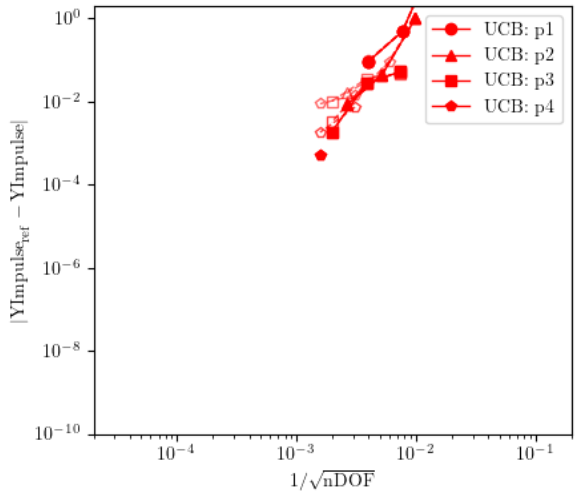

(a) Y-Impulse error - *coarser time resolutions indicated as increasing opacity's.*

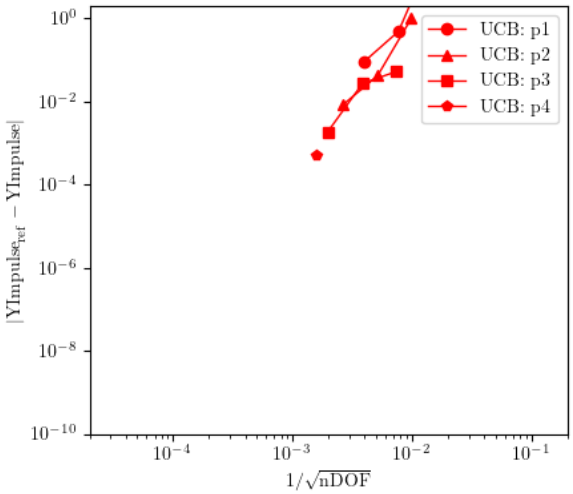

(b) Y-Impulse error - *finest time resolution*

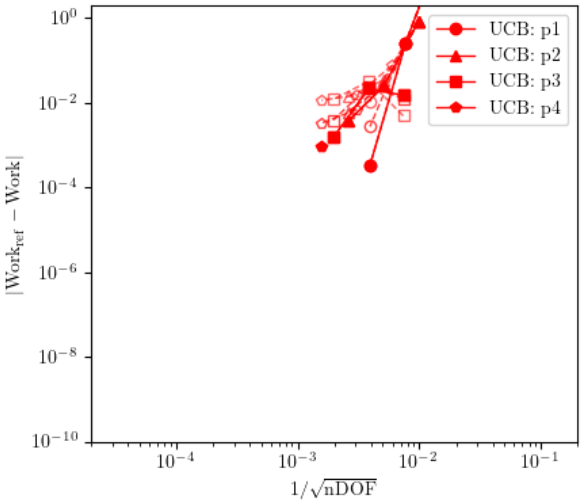

(c) Work error - *coarser time resolutions indicated as increasing opacity's.*

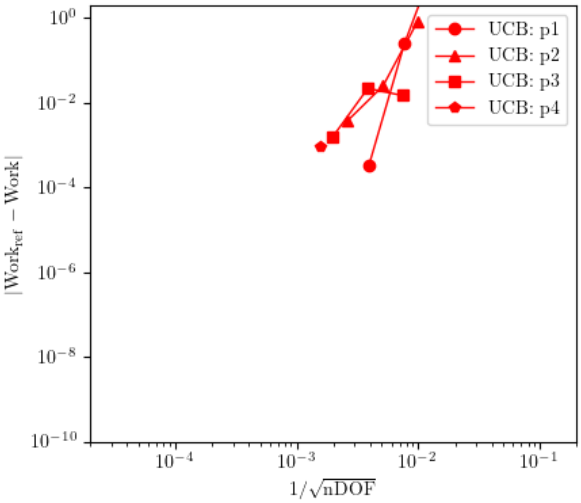

(d) Work error - *finest time resolution*

Figure 20: Airfoil Motion-4 (Heaving + Pitching, $M = 0.01$) Spatial Convergence: *Left column - time-discretization resolution studies plotted as increasingly opaque data sets. Increased opacity associated with less time-resolution. Right column - finest temporal resolution data-sets only for each group. (Truth data set: U. C. Berkeley)*

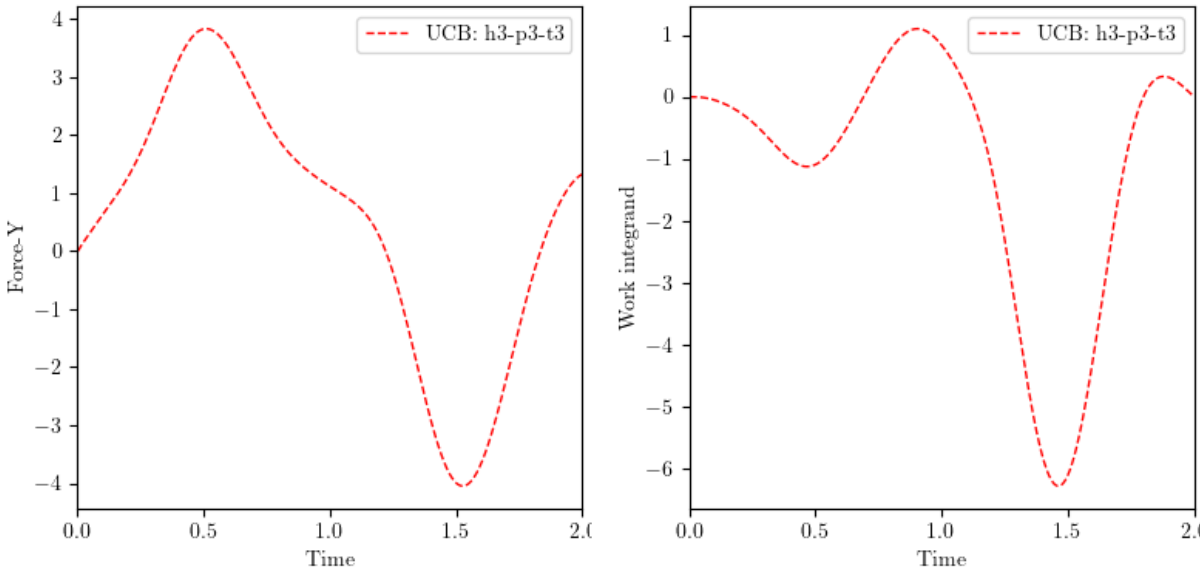

(a) Y-Force **(b) Work integrand**

Figure 21: Airfoil Motion-4 (Heaving + Pitchin, $M = 0.01$) Time Histories (finest space-time resolution data-sets from each participant)

A. Appendix A: Participant Convergence Studies

A. Flow in a cylinder

1. *Motion-1: short-time*

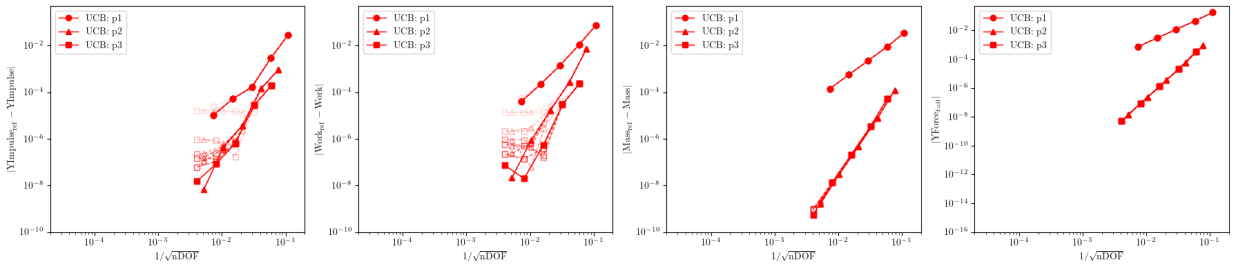

(a) U.C. Berkeley

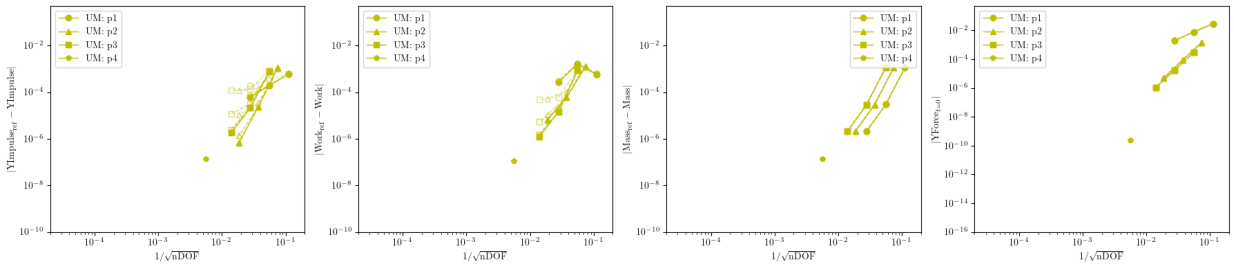

(b) University of Michigan

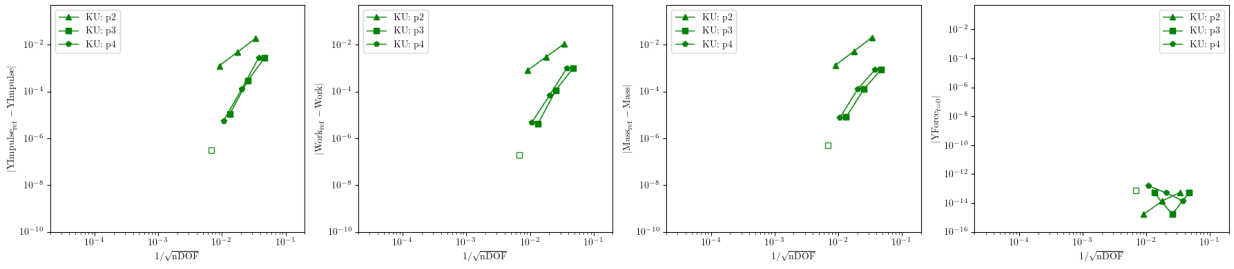

(c) University of Kansas

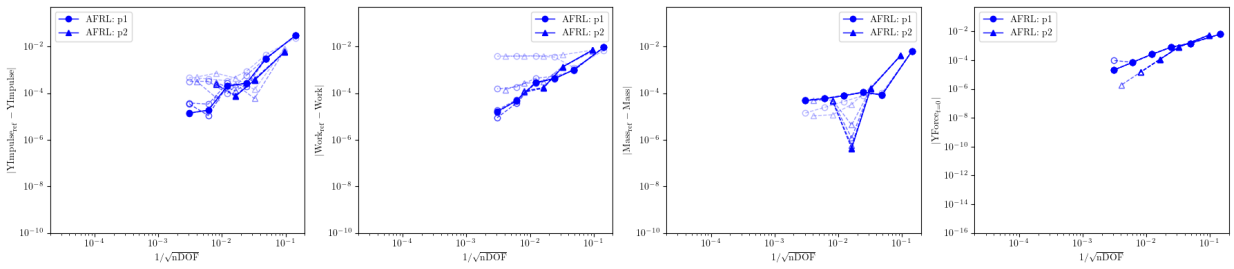

(d) Air Force Research Laboratory

Figure 22: Cylinder Motion-1 (short-time) Convergence for Y-Impulse, Work, Total Mass, and Initial Y-Force. Time-discretization resolution plotted as increasingly opaque data-sets. Increased opacity associated with less time-resolution. (U.C. Berkeley as truth data)

2. *Motion-2: long-time*

B. Heaving + Pitching Airfoil

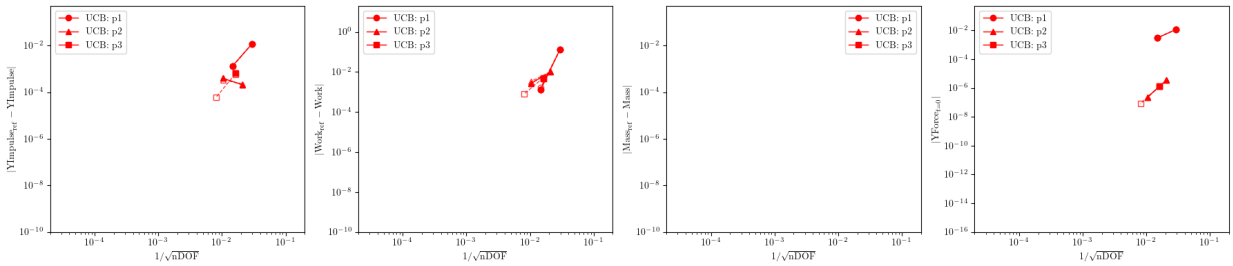

(a) U.C. Berkeley

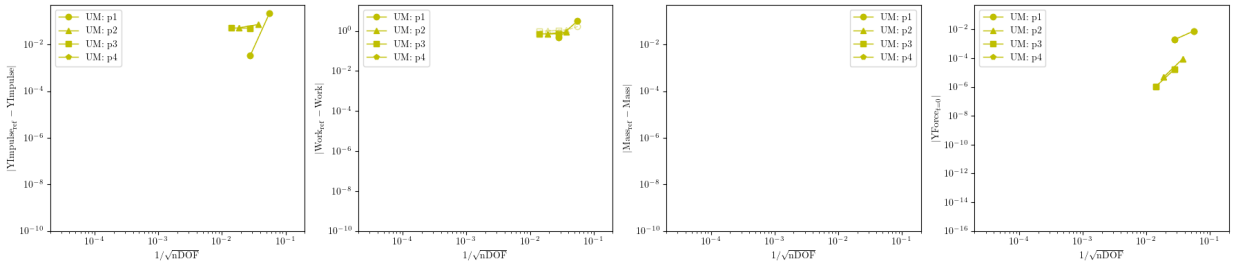

(b) University of Michigan

Figure 23: Cylinder Motion-2 (long-time) Convergence for Y-Impulse, Work, Total Mass, and Initial Y-Force. Time-discretization resolution plotted as increasingly opaque data-sets. Increased opacity associated with less time-resolution. (U.C. Berkeley as truth data)

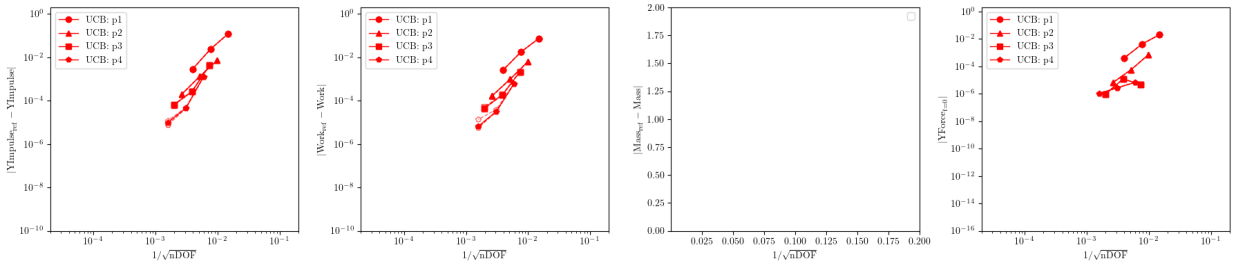

(a) U.C. Berkeley

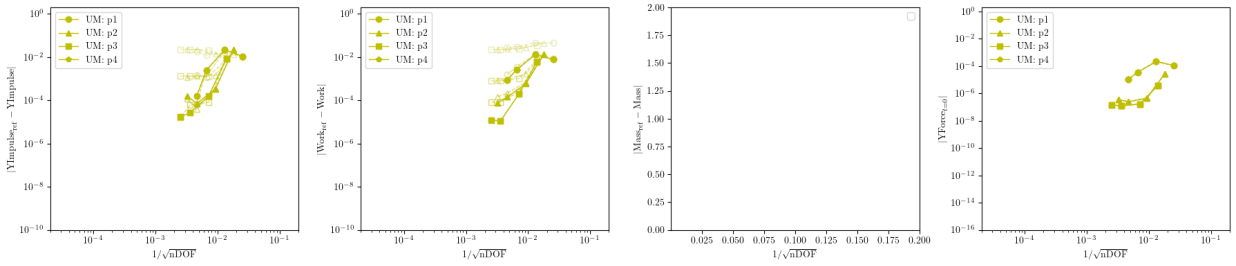

(b) University of Michigan

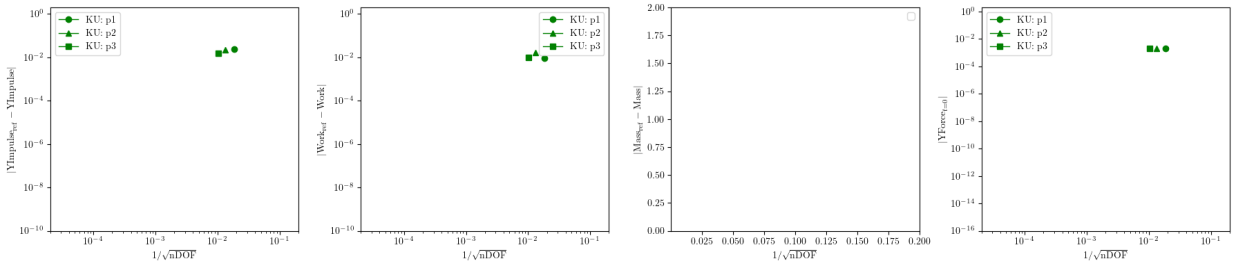

(c) University of Kansas

Figure 24: Airfoil Motion-1 (Heaving, Compressible) Convergence for Y-Impulse, Work, Total Mass, and Initial Y-Force. Time-discretization resolution plotted as increasingly opaque datasets. Increased opacity associated with less time-resolution. (U.C. Berkeley as truth data)

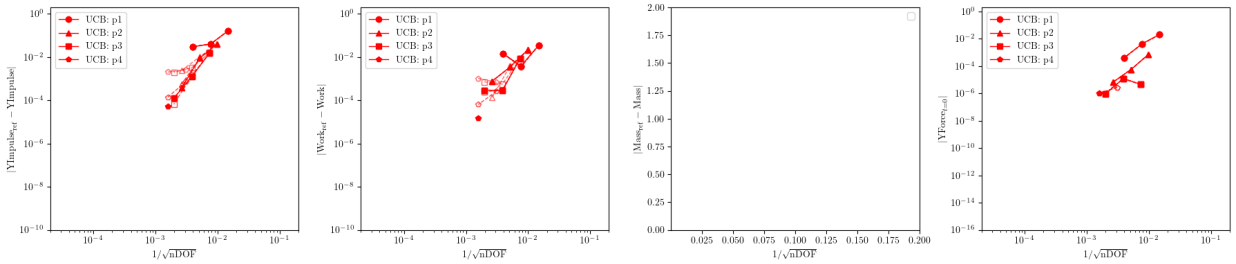

(a) U.C. Berkeley

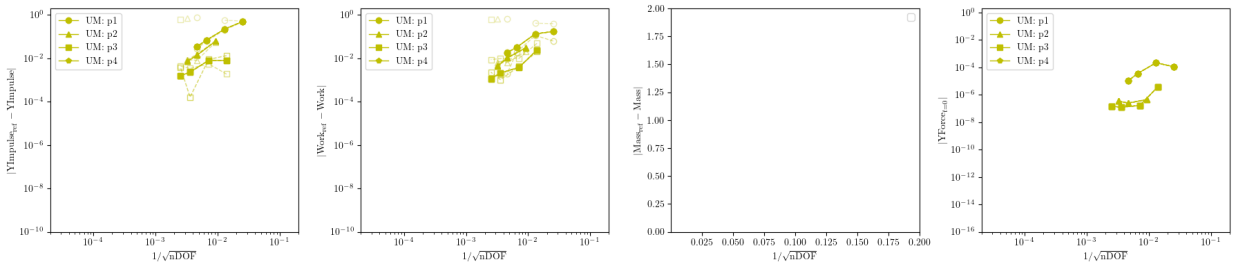

(b) University of Michigan

Figure 25: Airfoil Motion-2 (Heaving+Pitching, Compressible) Convergence for Y-Impulse, Work, Total Mass, and Initial Y-Force. Time-discretization resolution plotted as increasingly opaque data-sets. Increased opacity associated with less time-resolution. (U.C. Berkeley as truth data)

B. Appendix B: Details and modifications supporting incompressible test cases

A. Initial condition for a nearly incompressible cylinder testcase

For an ideal gas the sound speed, internal energy, and Mach number are related to the primitive variables via

$$c = \sqrt{\gamma \frac{p}{\rho}}, \quad e = \frac{1}{\gamma - 1}\frac{p}{\rho}, \quad M = \frac{u}{c}. \tag{8}$$

After some algebra to eliminate the sound speed,

$$e = \frac{u^2}{\gamma(\gamma-1)M^2} \quad \text{or} \quad M = \sqrt{\frac{\gamma(\gamma-1)e}{u^2}}. \tag{9}$$

While u varies throughout the simulation, we assume here that e is roughly constant, so that the maximum Mach number can be obtained from the initial internal energy and the maximum velocity. The latter can be estimated by running an incompressible simulation, which yields maximum velocity magnitudes of $u_1 = 2.10$ and $u_2 = 4.90$ for cylinder cases one and two respectively. For a target Mach number of $M = 0.01$, the resulting initial internal energy values are be

$$e_1 = 7.88 \times 10^4 \quad \text{and} \quad e_2 = 4.29 \times 10^5. \tag{10}$$

In this nearly incompressible limit the maximum kinetic energy density of the flow $k = \frac{1}{2}\rho u^2$ is much smaller than the internal energy, so that any change in internal energy due to mechanical or viscous effects from the flow should be negligible. Thus the initial internal energy is a good estimate for the internal energy at any point in the simulation, justifying our earlier assumption.

B. Details of MIT setup for the deforming cylinder

Below we specify the details of implementing the cylinder test case boundary deformation in the vorticity-velocity incompressible flow formulation of the MIT group. Here the focus is only on the boundary motion, as this is the only input to the simulation. We further define the force and work integrand expressions in terms of wall vorticity and wall vorticity flux, which avoids the need to evaluate the pressure explicitly.

We label the material points of the boundary by an angular coordinate θ, and define the position of each material point at time t as $\mathbf{x}(t,\theta)$. Let $\mathbf{k}$ indicate the out-of-plane unit vector. As preliminaries, note the arc length of a boundary segment of reference length $d\theta$ located at reference coordinate θ is given by $\mathrm{d}s = |\partial_\theta \mathbf{x}(t,\theta)|\,\mathrm{d}\theta$. Further, the normal and tangential unit vectors on the boundary at $\mathbf{x}(t,\theta)$ are

$$\boldsymbol{\tau}(t,\theta) = \frac{\partial_\theta \mathbf{x}(t,\theta)}{|\partial_\theta \mathbf{x}(t,\theta)|}, \quad \mathbf{n}(t,\theta) = \boldsymbol{\tau}(t,\theta) \times \hat{\mathbf{k}}. \tag{11}$$

Finally, the velocity of point θ at time t is $\mathbf{u}(t,\theta) = \partial_t \mathbf{x}(t,\theta)$.

1. *Boundary motion in Eulerian coordinates*

To describe the cylinder boundary motion, we define the rotation and deformation matrices

$$R(\gamma) = \begin{bmatrix} \cos(\gamma) & -\sin(\gamma) \\ \sin(\gamma) & \cos(\gamma) \end{bmatrix}, \quad D(t) = \begin{bmatrix} \phi(t) & \\ & \phi(t)^{-1} \end{bmatrix} \tag{12}$$

and note that the time derivatives of the deformation matrix are given explicitly by

$$D'(t) = \begin{bmatrix} \phi'(t) & \\ & -\phi(t)^{-2}\phi'(t) \end{bmatrix}, \quad D''(t) = \begin{bmatrix} \phi''(t) & \\ & 2\phi(t)^{-3}\phi'(t)^2 - \phi(t)^{-2}\phi''(t) \end{bmatrix}. \tag{13}$$

Define also the undeformed position $\mathbf{x}_0(\theta) = [r_0\cos(\theta),\, r_0\sin(\theta)]$. The position of each boundary point defined by material coordinate θ and time t is then

$$\mathbf{x}(t,\theta) = R(\theta_b(t))D(t)\mathbf{x}_0(\theta) + \mathbf{x}_c(t). \tag{14}$$

This expression can be easily inverted to obtain the material coordinate $\theta(t, \mathbf{x})$ from a given Eulerian boundary point at $\mathbf{x}$, at a given time t.

Dropping the t and θ dependence for simplicity, the velocity of the boundary is then given by

$$\mathbf{u}_b = \mathbf{u}_{\text{def}} + \omega_b \hat{\mathbf{k}} \times (\mathbf{x} - \mathbf{x}_c) + \mathbf{u}_c, \quad \text{with} \quad \mathbf{u}_{\text{def}}(t, \theta) = R(\theta_b(t)) D'(t) \mathbf{x}_0(\theta). \tag{15}$$

After defining the body acceleration $\mathbf{a}_c(t) = \mathbf{u}_c'(t)$, the angular acceleration $\alpha_b(t) = \omega_b'(t)$, and the deformation acceleration $\mathbf{a}_{\text{def}}(t, \theta) = R(\theta_b(t)) D''(t) \mathbf{x}_0(\theta)$, the boundary acceleration can be written as

$$\mathbf{a}_b = \mathbf{a}_{\text{def}} + \alpha_b \hat{\mathbf{k}} \times (\mathbf{x} - \mathbf{x}_c) - \omega_b^2 (\mathbf{x} - \mathbf{x}_c) + 2\omega_b \hat{\mathbf{k}} \times \mathbf{u}_{\text{def}} + \mathbf{a}_c, \tag{16}$$

where the terms in order represent the acceleration of the deformation, the angular acceleration, the centrifugal force, the coriolis force, and the body acceleration.

2. *Streamfunction*

In terms of arc-length parametrization $s(t, \theta)$, we seek a boundary stream function satisfying $\partial_s \psi(t, s) = \mathbf{u}(t, s) \cdot \mathbf{n}(t, s)$, which can be guaranteed with the definition

$$\psi(t, \theta') = \int_0^{\theta'} \partial_t \mathbf{x}(t, \theta) \times \partial_\theta \mathbf{x}(t, \theta) \, \mathrm{d}\theta \tag{17}$$

Evaluating the integrals we find that, up to rigid body motion,

$$\partial_t \mathbf{x}(t, \theta) \times \partial_\theta \mathbf{x}(t, \theta) = r_0^2 \frac{\phi'(t)}{\phi(t)} \left[\cos^2(\theta) - \sin^2(\theta)\right] = -r_0^2 \frac{\phi'(t)}{\phi(t)} \cos(2\theta) \tag{18}$$

The corresponding contribution of the surface deformation to the streamfunction can be found by integrating once with respect to θ, giving

$$\psi(t, \theta) = -\frac{r_0^2}{2} \frac{\phi'(t)}{\phi(t)} \sin(2\theta). \tag{19}$$

Adding this to the rigid body contribution of the boundary motion, we obtain the the full streamfunction

$$\psi(t, \mathbf{x}) = \mathbf{u}_c(t) \times (\mathbf{x} - \mathbf{x}_c(t)) - \frac{1}{2} \omega_b(t) \|\mathbf{x} - \mathbf{x}_c(t)\|^2 - \frac{r_0^2}{2} \frac{\phi'(t)}{\phi(t)} \sin(2\theta(t, \mathbf{x})). \tag{20}$$

3. *Force expression*

For an incompressible fluid with a no-slip boundary condition, the surface traction can be written as

$$\mathbf{f} = -p\mathbf{n} + \nu\omega\boldsymbol{\tau} + 2\nu\mathbf{k} \times \partial_s \mathbf{u}_b. \tag{21}$$

Integrating gives $\mathbf{F} = \oint_S \mathbf{f} \, \mathrm{d}s$ with $\mathbf{F} = \mathbf{F}_p + \mathbf{F}_v$, where the integral of the third term in equation (21) is zero for area preserving deformations. The viscous force,

$$\mathbf{F}_v = \nu \oint_S \omega \boldsymbol{\tau} \, \mathrm{d}s \,, \tag{22}$$

can be computed directly from the surface vorticity. For the pressure force we can write

$$\mathbf{F}_p = -\oint_S p\mathbf{n} \, \mathrm{d}s = \oint (\mathbf{x} \times \mathbf{k}) \partial_s p \, \mathrm{d}s \tag{23}$$

$$= \oint (\mathbf{x} \times \mathbf{k}) \left(\nu \partial_n \omega - \mathbf{a}_b \cdot \boldsymbol{\tau}\right) \mathrm{d}s \,, \tag{24}$$

which can be evaluated from the computed vorticity flux and the acceleration defined above.

4. Work integrand expression

The power applied to a deforming body by fluid forces can be written as the surface integral

$$P = \oint_S \mathbf{u}_b(t,s) \cdot \mathbf{f}(t,s)\,\mathrm{d}s\,, \tag{25}$$

where $\mathbf{f}(t,s)$ is the surface traction acting at each point on the body. Given (21), the total power can be broken into three integrals,

$$P = -\oint_S p(\mathbf{u}_b \cdot \mathbf{n})\,\mathrm{d}s + \nu \oint_S \omega(\mathbf{u}_b \cdot \boldsymbol{\tau})\,\mathrm{d}s + 2\nu \oint_S \partial_s \mathbf{u}_b \times \mathbf{u}_b\,\mathrm{d}s\,, \tag{26}$$

representing contributions from traction from pressure, vorticity, and surface kinematics respectively. Noting that $\mathbf{u}_b \cdot \mathbf{n} = \partial_s \psi$, the first integral can be integrated by parts to yield

$$P_p = \oint_S \psi \partial_s p\,\mathrm{d}s \tag{27}$$

$$= \nu \oint_S \psi \partial_n \omega\,\mathrm{d}s - \oint_S \psi(\mathbf{a}_b \cdot \boldsymbol{\tau})\,\mathrm{d}s\,, \tag{28}$$

which can be evaluated from the vorticity flux $\partial_n \omega$ and the expressions in the previous section. The second integral in (26) can be computed from wall vorticity and boundary kinematics. The third integral in (26) is given as

$$\begin{aligned}
P_b &= 2\nu \oint_S \partial_s \mathbf{u}_b \times \mathbf{u}_b\,\mathrm{d}s \\
&= 2\nu \oint_S \partial_s(\mathbf{u}_b + \mathbf{u_c} + \omega_b \hat{\mathbf{k}} \times (\mathbf{x} - \mathbf{x}_c)) \times (\mathbf{u}_b + \mathbf{u_c} + \omega_b \hat{\mathbf{k}} \times (\mathbf{x} - \mathbf{x}_c))\,\mathrm{d}s \\
&= 2\nu \oint_S \partial_s \mathbf{u}_b \times \mathbf{u}_b\,\mathrm{d}s + \omega_b \oint_S \partial_s \mathbf{u}_b \times (\hat{\mathbf{k}} \times (\mathbf{x} - \mathbf{x}_c))\,\mathrm{d}s - \omega_b \oint_S \mathbf{n} \times \mathbf{u}_b\,\mathrm{d}s - \oint_S \omega_b^2 \mathbf{n} \times (\mathbf{k} \times (\mathbf{x} - \mathbf{x}_c))\,\mathrm{d}s \\
&= 2\nu \oint_S \partial_s \mathbf{u}_b \times \mathbf{u}_b\,\mathrm{d}s - 2\omega_b \oint \mathbf{u}_b \cdot \boldsymbol{\tau}\,\mathrm{d}s + 2\omega_b^2 A_b,
\end{aligned} \tag{29}$$

where A_b is the (constant) area of the body. All three terms of P_b can be precomputed given the rigid-body motion and boundary deformation. The first term can be further simplified as

$$\begin{aligned}
\oint_S \partial_s \mathbf{u}_b \times \mathbf{u}_b\,\mathrm{d}s &= \int_0^{2\pi} \partial_\theta \partial_t \mathbf{x}(t,\theta) \times \partial_t \mathbf{x}(t,\theta)\,\mathrm{d}\theta \\
&= \int_0^{2\pi} r_0^2 \phi(t)^{-2} \phi'(t)^2 \sin^2(\theta) + r_0^2 \phi(t)^{-2} \phi'(t)^2 \cos^2(\theta)\,\mathrm{d}\theta \\
&= 2\pi r_0^2 \left(\frac{\phi'(t)}{\phi(t)}\right)^2.
\end{aligned} \tag{30}$$